A new high-resolution stratigraphic and palaeoenvironmental record spanning the End-Permian Mass Extinction and its aftermath in central Spitsbergen, Svalbard

V. Zuchuat[a,*], A.R.N. Sleveland[a], R.J. Twitchett[b], H.H. Svensen[c], H. Turner[d], L.E. Augland[c], M.T. Jones[c], Ø. Hammer[d], B.T. Hauksson[e], H. Haflidason[f], I. Midtkandal[a], S. Planke[c,g]

[a] Department of Geosciences, University of Oslo, Sem Sælands Vei 1, 0371 Oslo, Norway
[b] Natural History Museum, Earth Sciences Department, SW7 5BD London, UK
[c] Centre for Earth Evolution and Dynamics (CEED), Department of Geosciences, University of Oslo, Sem Sælands Vei 1, 0371 Oslo, Norway
[d] Natural History Museum, University of Oslo, Pb. 1172 Blindern, 0318 Oslo, Norway
[e] Geodata AS, Schweigaards gate 28, 0191 Oslo, Norway
[f] Department of Earth Science, University of Bergen, Allegate 41, 5020 Bergen, Norway
[g] Volcanic Basin Petroleum Research (VBPR), Høienhald, Blindernveien 5, 0361 Oslo, Norway

ARTICLE INFO

ABSTRACT

Research on the Permian-Triassic boundary (PTB) along the northern margins of Pangaea (exposed today in the Arctic region) has been heavily reliant on field observations, where data resolution was consequently determined by outcrop condition and accessibility. Core drilling in central Spitsbergen allowed for a near-complete recovery of two ~90 m cores through the PTB. Analyses of the core and nearby outcrops include stratigraphic logging and sampling, XRF scanning, petrography, biostratigraphy, isotope geochemistry, and geochronology. The First Appearance Datum (FAD) of *H. parvus* in Svalbard places the base of the Triassic *ca.* 4 m above the base of the Vikinghøgda Formation, and *ca.* 2.50 m above the End-Permian Mass Extinction (EPME) and its associated sharp negative δ^{13}C. The PTB therefore falls within the *Reduviasporonites chalastus* Assemblage Zone in Svalbard. Precise U-Pb TIMS dating of two zircon crystals in a tephra layer just above the first documented *Hindeodus parvus* in Svalbard gives an age of 252.13 ± 0.62 Ma. High-resolution palaeoenvironmental proxies, including Si/kcps (kilo counts per second), Zr/Rb, K/Ti, Fe/K, and V/Cr, indicate a transition towards a more arid climate in the earliest Triassic, contemporaneous with prolonged bottom-water dysoxic/anoxic conditions, following an increase in volcanic activity in the Late Permian. Statistical analysis of Zr/Rb, K/Ti and V/Cr elemental ratios suggests that the system was impacted by long-eccentricity (400 kyr) cyclicity. The δ^{13}C excursion in organic carbon ($\delta^{13}C_{org}$) record signals a large negative carbon isotope excursion (CIE) associated with the mass extinction event, but also records a second, smaller negative CIE *ca.* 22 m above this interval. This younger $\delta^{13}C_{org}$ excursion correlates to similar CIEs in the Dienerian (late Induan) records of other sections, notably in the Tethys Ocean, which have been interpreted as recording a small biotic crisis during the post-extinction recovery. Evidence of this negative CIE in Spitsbergen suggests that the Dienerian crisis may have been global in extent. The negative $\delta^{13}C_{org}$ values are associated with evidence for dysoxia or anoxia in the core, and the occurrence of tephra layers in the same interval suggests a possible connection between the Dienerian crisis and a discrete episode of volcanic activity.

1. Introduction

The PTB has been the focus of intense scientific study since the end of the nineteenth century (Baud, 2014) as life on Earth nearly disappeared during what is known today as the End-Permian Mass Extinction (EPME; Wignall and Twitchett, 1996) *ca.* 252 Ma (Burgess et al., 2014). The EPME led to the synchronous loss (Botha et al., 2020) of nearly 81% of marine species (Stanley, 2016) and 75% of terrestrial species (Hochuli et al., 2010) in <60 ± 48 kyr (Burgess and Bowring, 2015). Despite this wealth of scientific study, the exact cause(s) of this cataclysm remain disputed (Korte and Kozur, 2010; references therein). One of the primary candidates for driving the mass extinction are the

concomitant eruptions and intrusions of the Siberian Traps Large Igneous Province (LIP). The colossal volumes of volatile degassing from magmatic and contact metamorphic sources during the Siberian Traps formation are interpreted to have had a global impact on the chemistry and temperature of the atmosphere and hydrosphere (Svensen et al., 2009; Hochuli et al., 2010; Korte and Kozur, 2010; Ivanov et al., 2013; Black et al., 2014; Grasby et al., 2015). Environmental disruptions included global warming, sea surface temperature increase, ocean acidification, increased nutrient and sediment fluxes to the oceans, atmospheric ozone destruction, and widespread pulses of marine euxinia and anoxia (Wignall and Twitchett, 1996; Kidder and Worsley, 2004; Svensen et al., 2009; Joachimski et al., 2012; Clarkson et al., 2015; Dustira et al., 2013; Grasby et al., 2013; Wignall et al., 2016; Bond and Grasby, 2017; Stordal et al., 2017; Burger et al., 2019; Schobben et al., in press). These dramatic changes were contemporaneous with a sharp yet sustained negative carbon isotope excursion (CIE; Korte and Kozur, 2010).

The base of the Triassic is defined by its Global Stratotype Section and Point (GSSP), which is the first appearance (FAD) of the conodont *Hindeodus parvus* in the Meishan section, China (Yin et al., 2001). It has an inferred radiometric age of 251.902 ± 0.024 Ma (Burgess et al., 2014). The GSSP has its limitations, as it was defined within a condensed Tethyan limestone section. This prevents high-resolution palaeoenvironmental proxy analyses and correlations between sections, both in South China (Baresel et al., 2017) and further afield (*e.g.*, East Greenland; Twitchett et al., 2001). The former northern margins of Pangaea (Canadian Arctic, East Greenland, and Barents Shelf) offer ideal study material for Permian Triassic successions as these sections are both stratigraphically expanded and siliciclastic-dominated, which allows the implementation of high-resolution analyses (*e.g.* Tozer, 1965, 1967; Mørk et al., 1993; Mørk et al., 1999a; Mørk et al., 1999b; Twitchett et al., 2001; Beauchamp and Baud, 2002; Wignall and Twitchett, 2002; Beauchamp et al., 2009; Grasby and Beauchamp, 2008, 2009; Dustira et al., 2013; Grasby et al., 2013, 2015, 2016, 2019). These sections are typified by silica-rich, sometimes cherty or spiculitic, bioturbated mudstones and sandstones in the Late Permian. These successions transitioned to silica-poor, usually laminated, and easily-weathered mudstones across the PTB. In Canada and in Greenland, the FAD of *H. parvus* occurs some metres above the base of this lithological transition (Twitchett et al., 2001; Grasby and Beauchamp, 2008; Beauchamp et al., 2009).

Previous research on the PTB in the Arctic region has mostly relied on field observations and sampling from outcrops, where resolution was dependent on outcrop quality and accessibility. This study reports on two 90 m cored marine sedimentary successions intersecting the PTB in Deltadalen, central Spitsbergen (Fig. 1). The cores, coupled with an equivalent outcrop 1 km northeast of the borehole (Deltadalen river section, Fig. 1), yield high-quality, comprehensive and time-calibrated multidisciplinary data through the targeted stratigraphic interval at a resolution not previously achieved in the Arctic. We integrate detailed sedimentary logs of the cores, high-resolution colour and hyperspectral photographs, XRF core scanning results, three-dimensional (3D) microcomputer tomography data, and organic geochemistry data. The aim of this study is to conduct high-resolution analyses of bio-sedimentary indicators of palaeoenvironmental change through the PTB, reflecting changes in parameters such as climate, continental weathering and influx, dissolved oxygen levels, and organic productivity in the water column.

2. Geological framework

Svalbard is situated on the uplifted northern corner of the Barents Sea Shelf, displaying the onshore portion of the otherwise subcropping stratigraphic succession (Dallmann, 1999). It has thus been used as an analogue for the Barents Sea Shelf, as both domains have shared a common tectono-depositional history since before the breakup of Pangaea (Worsley, 2008; Smelror et al., 2009). The semi-continuous Precambrian-Quaternary stratigraphic succession, punctuated by hiatuses, records major tectonic events, sea-level changes and extinction episodes.

The Permian is characterised by peak growth rates of the Ural Orogeny, as the Uralian Seaway was closing (Blomeier et al., 2011). The Uralian and Barents waters became increasingly isolated from the Tethys Ocean, and siliciclastic sediment input increased through the Permian until the Wordian-Wuchiapingian (Reid et al., 2007). The Upper Permian Kapp Starostin Formation (Cutbill and Challinor, 1965) was deposited in broad epicontinental depocentres separated by structural highs, with an overall basin-shallowing towards the Sørkapp-Hornsund High to the south and the Nordaustlandet Platform to the northeast (Birkenmajer, 1977; Malkowski, 1982; Lipiarski and Čmiel, 1984; Wendorff, 1985; Dallmann et al., 1999; Uchman et al., 2016). The Kungurian Vøringen Member at the base of the Kapp Starostin Formation consists of bioclastic, light-coloured limestone strata, containing corals, brachiopods, crinoids and bryozoans (Ehrenberg et al., 2001; Blomeier et al., 2013). It was deposited in a shoreface position on a storm-dominated ramp (Dallmann et al., 1999; Blomeier et al., 2011; Jafarian et al., 2017). The overlying Kungurian(?) – Capitanian Svenskeega Member (Cutbill and Challinor, 1965), which was deposited on an open marine, storm-dominated shelf, comprises spiculitic mudstones with occasional quartz sandstone beds (Harland and Geddes, 1997). The uppermost Stensiöfjellet Member in central Spitsbergen is a glauconite-rich, fine- to coarse-grained cherty sandstone with occasional brachiopod-bearing limestone beds that was deposited in an upper shoreface to foreshore system (Blomeier et al., 2013). It transitions laterally into the shelfal, mud- and siltstone-dominated Hovtinden and Revtanna members to the north and south, respectively (Blomeier et al., 2013).

In western Spitsbergen, the lithological boundary between the Kapp Starostin Formation and the overlying Vardebukta Formation is a sharp, possibly erosive boundary between spiculitic and non-spiculitic mudstones (Mørk et al., 1999b). Likewise, in central Spitsbergen an erosive contact has been inferred at the base of the Vikinghøgda Formation, as defined by Mørk et al. (1999a), but the evidence for this has been questioned by Nabbefeld et al. (2010). There is no evidence of major breaks in sedimentation within the Kapp Starostin Formation, but several authors discuss the idea that the Changhsingian is not recorded by fossil data and could be missing (Buchan et al., 1965; Mørk et al., 1982; Nabbefeld et al., 2010; Vigran et al., 2014). A similar transition from silica-rich to silica-poor lithologies is also observed between the Permian Black Stripe Formation and the Upper Permian to Lower Triassic Blind Fiord Formation in the Canadian Arctic (Grasby and Beauchamp, 2009; Algeo et al., 2012; Grasby et al., 2013; references therein). The exact cause of this facies change remains unresolved, but it may reflect the Early Griesbachian onset of rifting that initiated the breakup of Pangaea (Seidler et al., 2004).

The overall Triassic stratigraphy of Svalbard consists of nine upward-finning – upward-coarsening, transgressive – regressive (T-R) clastic cycles characterised by high sedimentation rates in a rapidly subsiding basin (Mørk et al., 1989; Vigran et al., 2014). The base of the Vardebukta Formation in western Spitsbergen and the Vikinghøgda Formation in central and eastern Spitsbergen is diachronous (Worsley and Mørk, 1978; Nakrem and Mørk, 1991; Mørk et al., 1999b; Worsley, 2008), flooding the Hornsund High in south Spitsbergen in the Olenekian only (Zuchuat, 2014).

Both the Vardebukta and Tvillingodden formations in western Spitsbergen, and the Vikinghøgda Formation in central Spitsbergen and eastern Svalbard, are characterised by dark-grey, open marine to inner shelf mudstones, containing a variable yet low amounts of organic matter. The mudstones are interbedded with bioturbated event beds such as storm-influenced hummocky cross-stratified sandstones, hyperpycnite-sourced siltstones and very fine-grained sandstones (Mørk et al., 1999b; Wignall et al., 2016; Jelby et al., 2020). Calcareous
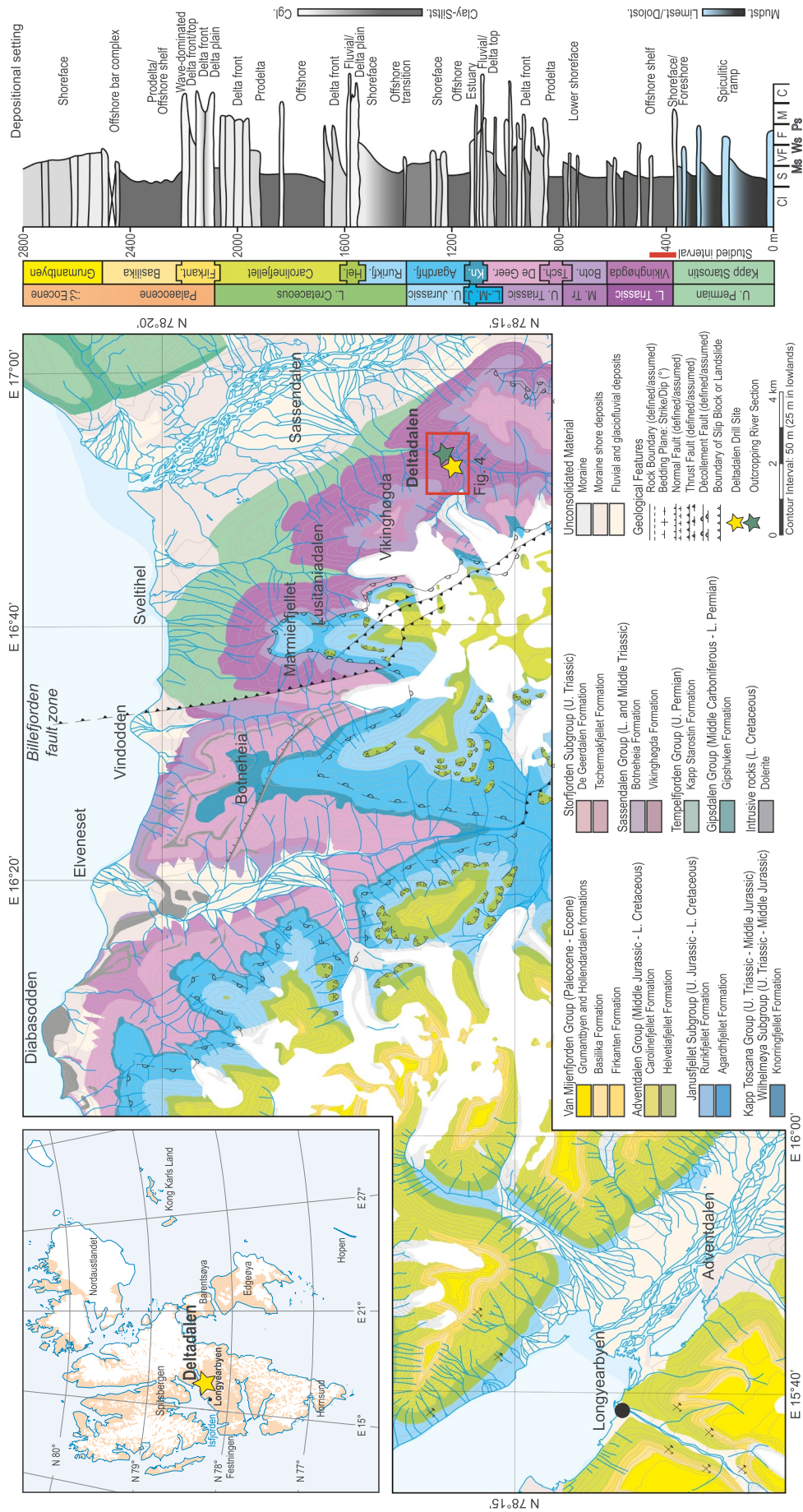
(caption on next page)

Fig. 1. Map and geological map indicative of the drill site (yellow star) and the neighbouring Deltadalen river section (green star; geological map modified from Major et al., 1992). Summary sedimentary section of the lithostratigraphical formations on central Spitsbergen (after Dallmann et al., 1999; Mørk et al., 1999b; Midtkandal et al., 2008; Nagy and Berge, 2008; Dypvik et al., 2011; Blomeier et al., 2013; Lord et al., 2014; Koevoets et al., 2016; Smelror and Larssen, 2016). (For interpretation of the references to colour in this figure legend, the reader is referred to the web version of this article.)

nodular horizons contain remains of gastropods, bivalves, bryozoans, fish bones, conodonts and ammonoids (Nakrem and Mørk, 1991; Foster et al., 2017b). The amount of bioturbation, the frequency of occurrence of fossil remains, and the occurrence and thickness of event beds all generally increase towards the top of each of these three formations, suggesting increased energy-levels linked to shallowing (Buchan et al., 1965; Mørk et al., 1982, 1989; Wignall et al., 1998; Foster et al., 2017b). A west-east transect from the Lower Triassic Vardebukta Formation to the Deltadalen Member of the Vikinghøgda Formation shows an eastward-deepening trend (Mørk et al., 1999b; Wignall et al., 2016; Hammer et al., 2019). Early Triassic shallow marine pro-delta environments dominated the western areas, recorded by the Vardebukta Formation, while deeper shelf mudstones are characteristic of the Deltadalen Member; the whole system being under the influence of a coastline prograding from the west/southwest to the east/northeast (Mørk et al., 1982; Mørk et al., 1999b; Wignall et al., 2016).

3. Material and methods

3.1. Sedimentology

Two cores, DD-1 and DD-2, were collected in Deltadalen (Fig. 1; UTM 33x: E0542440-N8688450), each reaching a depth of *ca.* 100 m below the surface (mbs). In order to improve total recovery of the cored interval, and to increase sampling volume, the second core DD-2 was drilled 2 m from DD-1. The uppermost 10 m of both cores consist of unconsolidated reworked material, while the remaining 90 m have nearly 100% recovery rate.

The recovered cores are 3.18 cm in diameter, and sampled two main lithostratigraphic units: 15 m of Upper Permian green, glauconitic, cherty sandstone (Upper Permian Stensiöfjellet Member of the Kapp Starostin Formation), which strongly contrasts with the spiculitic-mudstone-dominated succession observed at Festningen or the silica-rich Upper Permian strata elsewhere in the Arctic (Tozer, 1967; Mørk et al., 1993; Dallmann et al., 1999; Twitchett et al., 2001; Beauchamp and Baud, 2002; Wignall and Twitchett, 2002; Beauchamp et al., 2009; Grasby and Beauchamp, 2008, 2009; Grasby et al., 2013; Sanson-Barrera et al., 2015; Grasby et al., 2016). The upper ~75 m of the recovered cores consist of the Upper Permian to Lower Triassic (based on recovered conodonts and correlation to Burgess et al.'s (2014) carbon isotope curve; see below) mudstones of the Deltadalen and Lusitania-dalen members of the Vikinghøgda Formation (Mørk et al., 1999b). The cores were calibrated with dated tephra-horizons from the neighbouring Deltadalen River section (Fig. 1).

One of the cores (DD-1) was logged at mm-scale after it was split (Fig. 2). Standard techniques in lithofacies analysis and sedimentary architectural element analysis (Walker, 1992) were used in order to permit interpretation of depositional settings (Fig. 3). Bioturbation was quantified using the index of MacEachern et al. (2005), with 0 indicating undisturbed strata and 6 indicating thoroughly bioturbated sediments. A first-order stratigraphic description identified three carbonate-cemented concretion levels that serve as marker beds for the lower outcrop section (Fig. 4). The photographs of the split core, as well as the detailed sedimentary log are available as Supplementary material to this article. In order to help identify the degree of bioturbation within the mudstones in the core, micro-computer tomographs of targeted intervals were produced (Fig. 5). This dataset was complemented by a 10 m photographed and measured sedimentary section exposed in the banks of the Deltadalen River, *ca.* 1 km NE of the drill site (UTM 33x: E0542948-N8689445; Fig. 4B). About 100 kg of concretion material

was also collected from the Deltadalen river section, parts of which were dissolved in order to collect and identify microfossils including conodonts.

3.2. U-Pb geochronology

Eight tephra samples of *ca.* 10 kg each were collected from the Deltadalen river section, from which zircon crystals were extracted for U-Pb dating (Fig. 4B). Heavy minerals were separated by standard procedures including gravity settling and decanting, as well as magnetic and heavy liquid separation. Although abundant euhedral zircons were present in several samples, most were detrital and only the tephra at 2.49 m (just above concretion level 3; Fig. 4B) yielded euhedral magmatic zircons (*n* = 2) that potentially record the age of deposition of the tephra bed. These two zircons were chemically abraded and analysed by ID-TIMS at the Department of Geoscience at the University of Oslo. For detailed descriptions of analytical techniques see Ballo et al. (2019).

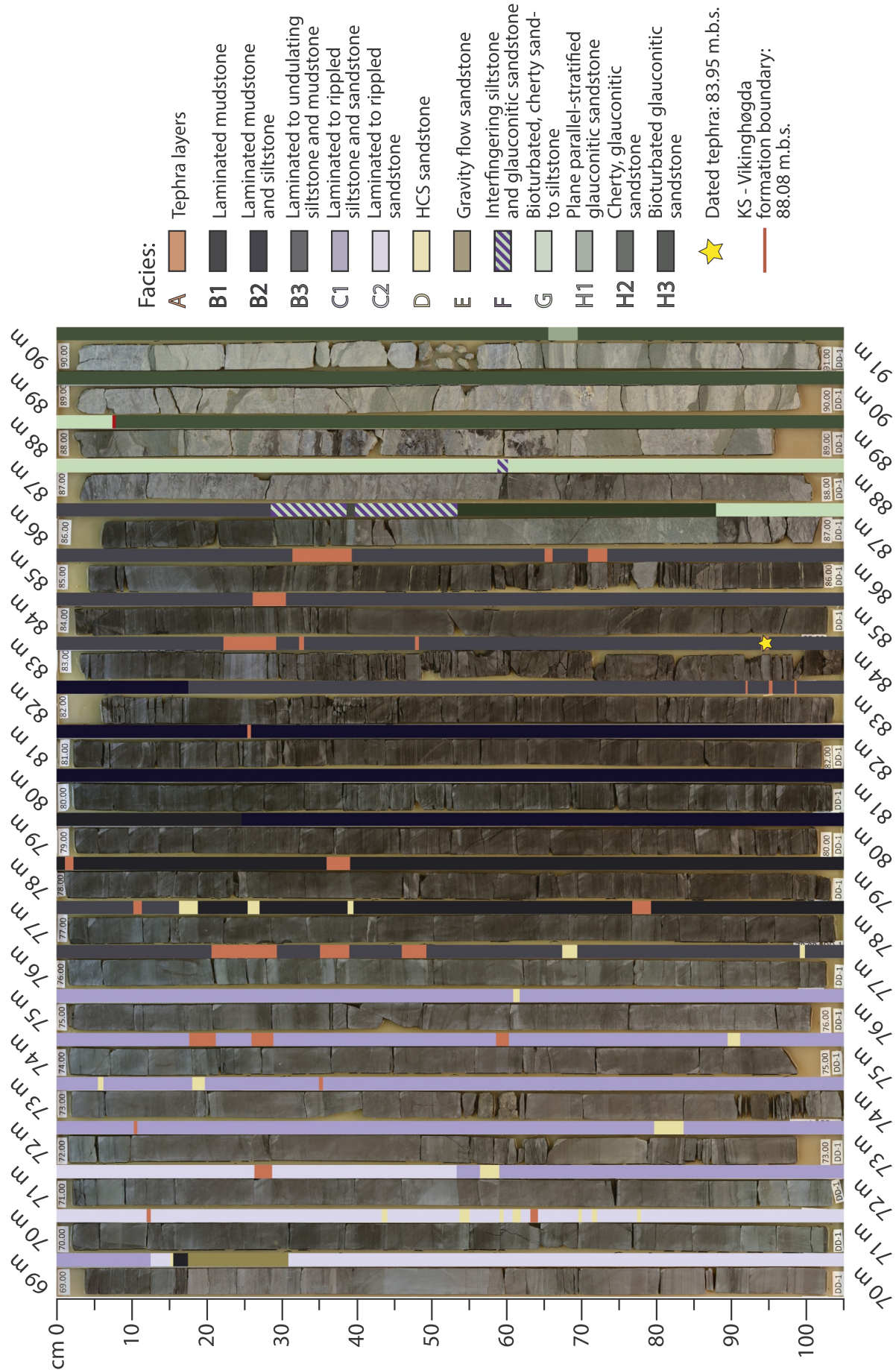### 3.3. Microscopy and electron microprobe analyses

Selected samples and thin sections from DD-1's twin core DD-2 were studied using Scanning Electron Microscopy (Hitachi SU5000 FE-SEM) and Electron Microprobe (Cameca SX100) at the Department of Geosciences, University of Oslo. The main purpose was to identify detrital and authigenic minerals in representative samples from the Kapp Starostin and Vikinghøgda formations (3 samples) and to verify the presence and composition of tephra layers (4 samples; Figs. 3, 6).

3.4. XRF core scanning and XRF analysis

Core DD-1 was analysed for bulk elemental composition on an ITRAX X-ray fluorescence (XRF) core scanner at the Department of Earth Science, University of Bergen. All runs were performed at room temperature with the Molybdenum X-ray tube, using fixed 30 kV and 30 mA settings. The overall analytical resolution was set to 500 μm, except for the interval between 75 m and 90 m which was scanned at a resolution of 200 μm, with a counting time of 10 s.

The raw XRF data were filtered with a Mean Standard Error (MSE) threshold value of 2.0, before normalizing selected elements against Fe and averaging the curves using a kernel regression method (Wand and Jones, 1994) in order to ease their readability on figures. Enrichment factors (EF) for selected trace metal were calculated following Woitke et al. (2003) equation. Elemental concentrations were normalised against background concentrations. These background concentration values were calculated for both the Kapp Starostin and the Vikinghøgda formations. The raw XRF data are available in Supplementary materials.

Guided by sedimentary facies analysis, 11 additional representative samples were collected from DD-1. These samples were analysed for their bulk elemental composition and used to calibrate the XRF scan data set. The samples were analysed by XRF at Chemostrat Ltd. (UK). Each of them were ground to below 50 μm, after which 4 g of ground powder was mixed with 0.4 g of wax binder. The XRF data of the sample set was pre-calibrated with 40 reference materials including numerous international rock standards. In addition, all elemental interferences have been tested and accounted for in the software algorithms *e.g.* Ba interference on TiO_2. A batch of standards were analysed every 20 samples or less, which values were then compared against the true reference value of each standards, after which a correction factor

Facies:

- A — Tephra layers
- **B1** — Laminated mudstone
- **B2** — Laminated mudstone and siltstone
- **B3** — Laminated to undulating siltstone and mudstone
- C1 — Laminated to rippled siltstone and sandstone
- C2 — Laminated to rippled sandstone
- D — HCS sandstone
- E — Gravity flow sandstone
- F — Interfingering siltstone and glauconitic sandstone
- G — Bioturbated, cherty sandstone to siltstone
- H1 — Plane parallel-stratified glauconitic sandstone
- **H2** — Cherty, glauconitic sandstone
- **H3** — Bioturbated glauconitic sandstone

★ — Dated tephra: 83.95 m.b.s.

— KS – Vikinghøgda formation boundary: 88.08 m.b.s.

(caption on next page)

Fig. 2. Photographs of the core, sawed and facies coded, between 69 and 91 m.b.s. The formation boundary (red line) delimits the Kapp Starostin Formation from the Vikinghøgda Formation (Mørk et al., 1999a). (For interpretation of the references to colour in this figure legend, the reader is referred to the web version of this article.)

was produced.

3.5. Carbon isotope analysis and Rock-Eval

Total organic carbon (TOC) and Rock-Eval were analysed at Applied Petroleum Technology, Oslo, and carbon isotope analyses at the Institute for Energy Technology, Kjeller, Norway. A total of 152 samples for TOC measurements were hand crushed in a mortar and the powders decarbonated with diluted HCl. The samples were then placed in a Leco SC-632 combustion oven and the carbon measured as carbon dioxide by an IR-detector. A Rock-Eval 6 instrument was used for pyrolysis and Jet-Rock 1 was run as a standard between every tenth sample and checked against the acceptable range given in the Norwegian industry guide to organic geochemical analyses (NIGOGA). The temperature was held at 300 °C for 3 min and increased stepwise by 25 °C per min up to 650 °C.

For isotope analyses, 50–100 mg powdered rock was treated in 2 ml of 2 M HCl for 16 h to remove calcite and dolomite, followed by pipette removal of acid and washing three times with 5 ml DD water. The samples were dried over night at 80 °C before analyses a Nu® Horizon isotope ratio mass spectrometer. The results were plotted on a 2 point calibration line calculated from analysis of the USGS 24 standard (−16.05‰; United States Geological Survey) and an in-house graphite standard (−31.56‰) analysed in each sample sequence. The average reproducibility of duplicate standard analyses was ±0.04‰ for the second round of processed samples. For analytical control, a third standard, B2153 (−26.66‰) from Elemental Microanalysis, was run in all sample sequences and gave an average value of −26.89‰ ±0.14 with one standard deviation. All results are reported using the conventional δ-notation in per mil with respect to the Vienna Pee Dee Belemnite (VPDB).

3.6. Evolutionary spectral analysis

XRF elemental ratios curves were analysed using Li et al.'s (2019) Acycle software suite in order to identify cyclical patterns. Only the 55.22 m interval comprised between the tephra bed (U-Pb age) and the Induan-Olenekian boundary (251.22 ± 0.20 Ma; Burgess et al., 2014) were analysed, covering *ca.* 0.91 Myr. In order to conduct Evolutionary Spectral Analysis (ESA), the curve-sampling had to be equally spaced along the targeted interval, and one value was extracted each centimetre from the XRF table (see Supplementary material). Values were interpolated for intervals where the XRF scanner didn't record any value (maximum interpolated interval: 4 cm). The maximum frequency parameter of the ESA was set at 3, with a 10 m sliding window. Each ESA spectrograms is accompanied by 2π Multi-Taper Method (MTM) power spectrum, used to identify the wavelength of the major recognised cycles.

4. Results

4.1. Sedimentology

Following Walker's (1992) principles, eight facies (A-H) have been recognised in the core (Figs. 2, 3; Table 1). Facies B and C have each been further subdivided in three sub-facies depending on their sand-to-mud ratio. Facies H has also been subdivided in three sub-facies, according to varying chert content and bioturbation degree. The detailed descriptions and interpretations of each of these facies are included as Supplementary material. These eight facies have been grouped in two facies associations (FAs) separated by a transition zone represented by

Facies F (Figs. 2, 3, Table 1).
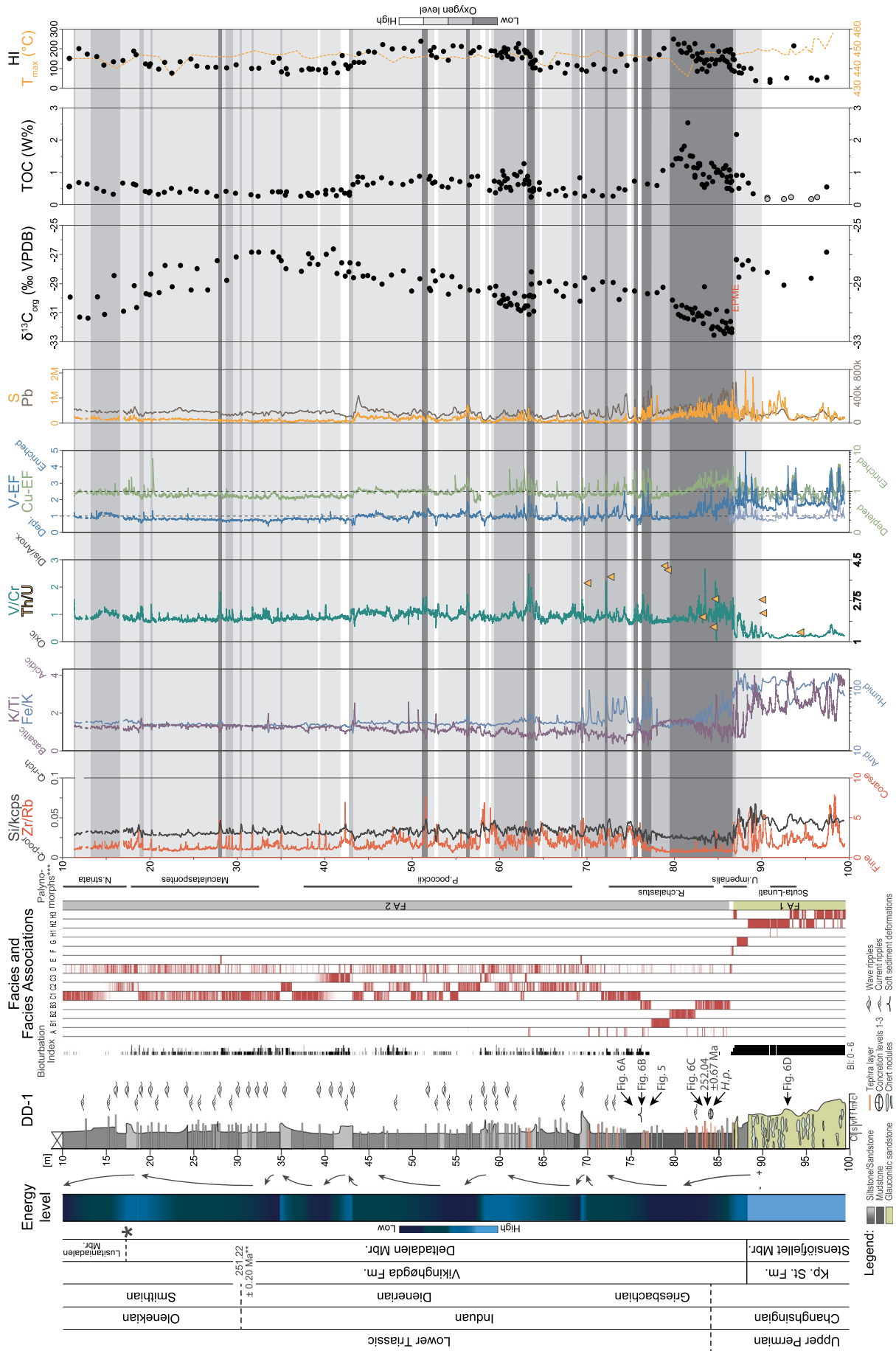
4.1.1. Facies association 1 – shoreface
4.1.1.1. Description. FA 1 is observed in the lowermost part of the core (Figs. 2 and 3). It comprises green glauconitic, fine- to medium-grained sandstone (Facies H1–3, Table 1) which belongs to the Stensiöfjellet Member of the Kapp Starostin Formation. Occasional primary plane parallel-stratifications (Facies H1) are commonly obliterated by secondary chert precipitation (Facies H2) or thorough bioturbation (*Zoophycos*, BI 5–6; Facies H3). At 88.08 m below the surface (m.b.s.), Facies H2 is sharply overlain by a dark grey to green, upward-fining very fine sandstone to siltstone interval (Facies G), which displays varying glauconite and chert content. Facies G is thoroughly bioturbated by *Phycosyphoniform* and *Zoophycos* (BI 5–6). The base of Facies G marks the base of the Vikinghøgda Formation *sensu* Mørk et al. (1999b). At 86.89 m.b.s., Facies G is sharply overlain by a 35 cm thick heavily bioturbated green sandstone bed (BI 6; Facies H3), which represents the uppermost strata of FA 1. The base of Facies H3 is not an erosive surface, but does display an irregular relief related to the presence of burrows, which transported some green glauconitic sand down into the siltstone of Facies G (Fig. 2). These burrows do not seem to have deformed the underlying siltstone strata of Facies G as they formed.

4.1.1.2. Interpretation. The high degree of bioturbation in FA 1 indicates elevated levels of oxygen in the system, in which the sediment supply was low enough to allow for animals to entirely colonise the first decimetres of the seafloor. The grain size (fine to medium) and occasional thin, plane parallel-laminated intervals reflect episodes of sediment transport by traction currents and related settling. The sharp transition from Facies H into Facies G, coupled with the upward-fining character of this facies, represents a rapid lowering of the system's energy level in response to likely deepening. The system recorded abrupt energy oscillations, with the deposition of Facies H3's heavily bioturbated glauconitic sandstones sharply overlying the finer-grained bioturbated sediments of Facies G. However, the undeformed nature of Facies G's uppermost strata directly juxtaposed to the burrows that developed from the overlying Facies H3 suggests that the uppermost layers of Facies G were already firm or stiffened as the burrows developed shortly after the deposition of Facies H3. The apparent stiffness or firmness of Facies G suggests that some condensation occurred between these two facies. The scarcity of preserved primary plane parallel-laminations, and the undiagnostic character of the ichnofacies, makes it hard to pinpoint the exact depositional setting of this unit. However, following the interpretation of Blomeier et al. (2013), these sediments are thought to have been deposited as part of an upper shoreface to foreshore system, which developed within the shallowest waters of a ramp opened onto the Boral Ocean.

4.1.2. Facies F – transgression from upper shoreface to offshore setting
4.1.2.1. Description. Facies F covers an interval between 86.54 and 86.29 m.b.s. (Figs. 2, 3, Table 1). Facies F marks the transition from FA 1 uppermost bioturbated glauconitic sandstone ledge (Facies G) into the deposits of FA 2. It consists of a complex stacking of green glauconitic sand and plane parallel-laminated siltstone. The bioturbation index is much lower than the underlying FA 1 deposits at 0 to 2, and the sand-to-mud ratio diminishes up section.

4.1.2.2. Interpretation. The decreasing sand-to-mud ratio over this interval testifies of a gradual lowering of system energy. The energy-

(caption on next page)

level must have remained episodically sufficiently high to re-mobilise and re-transport glauconitic sand. The bioturbation index reflects reduced oxygen levels with respect to the underlying thoroughly bioturbated FA 1. This interval is interpreted to reflect a rapid deepening.

4.1.3. Facies association 2 – offshore to offshore transition storm-wave-dominated shelf

4.1.3.1. Description. Facies association 2 comprises Facies A to Facies E (Figs. 2, 3, Table 1). Its base is defined at 86.29 m.b.s., where the uppermost green glauconitic sandstone of Facies F occurs. FA 2 is arranged in 6 upward-fining-to-upward-coarsening intervals (UF2UCIs; Fig. 3). It is dominated by non-spiculitic, laminated to undulating silt-to-mud-to-siltstone intervals up to *ca.* 76 m.b.s. (Facies B; Fig. 2, Table 1), coarsening up section to very fine-grained sandstone strata (Facies C; Table 1). Both Facies B and Facies C have been subdivided in three subfacies to reflect their respective varying sand-to-mud ratios and bioturbation degrees (Table 1). Facies B1 is the finest-grained facies of the entire core, as it nearly exclusively consists of laminated mudstone. Oscillations and unidirectional current ripples occasionally occur up to *ca.* 70 m.b.s., after which they become more common (Figs. 2 and 3). The frequency of 5–8 cm thick hummocky cross-stratified beds (HCS; Facies D) and other event beds generally increases from 77.30 m.b.s. towards the top of the core, with a notable interval between *ca.* 45 and 35 m.b.s. in which HCS beds are much more infrequent.

The interval between 86.29 and 69.32 m.b.s. represents the lowermost of these six UF2UCIs (Fig. 3). It comprises at least three hard-cemented intervals which were correlated to concretion levels in the neighbouring outcropping section (Fig. 4). It displays a gradual sand-to-mud ratio reduction, an increasing dominance of plane parallel-laminated mudstone as the scattered undulating silty and sandy strata disappear. This is coupled with a decreasing frequency in visible pyrite cluster occurrence, and a sharp decrease in the degree of bioturbation from 2 to 0.5 as it grades from Facies B3 into Facies B1 between 86.29 and 77.19 m.b.s. Note that the interval covered by Facies B2 and B1 contains no visible ichnofabric, but rare mm-scale burrows have been identified from micro-computer-tomography scans (Fig. 5). This interval also contains several bentonite-tephra layers (Facies A; Figs. 2 and 3; Table 1), some of which were correlated to the Deltadalen river section outcrop (Fig. 5). These tephra layers are concentrated within the deposits of Facies B3 at the base of FA 2 up until 83.23 m.b.s., and between 76.50 and 76.21 m.b.s. (Figs. 2 and 3). Only one thin tephra layer has been recorded in Facies B2, and none in Facies B1. Two thin tephra layers have also been identified at 63.38 m.b.s. within interval B (Fig. 3).

4.1.3.2. Interpretation. FA 2 is interpreted as recording the offshore to offshore transition of a storm-wave-dominated shelf that underwent a rapid transgression followed by a slow regression, similar to Bohacs et al. (2014)'s FA1-S. The maximum flooding surface (MFS; *sensu* Catuneanu et al., 2009) is located within the thinly laminated mudstone of Facies B1. The rapid sinking of the system at the base of FA 2 is contemporaneous of a drastic shift in life conditions on the seafloor at its base, as testified by the near-disappearance of bioturbation, coinciding with elevated evidence of volcanic activity. The position of the MFS in the core potentially parallels Seidler et al. (2004)'s lower Griesbachian climax of the Greenland-Norwegian Sea

rifting. The return of visible ichnofabric at 77.19 m.b.s. is accompanied by an increase in burrow size, which implies that the first centimetres of shelfal substratum became subsequently more oxygenated than they previously were (Nabbefeld et al., 2010; Hofmann et al., 2013; Foster et al., 2017b). This rapid recovery of life seems to contradict N-isotope data from the Festningen section, 72 km west of DD-1 drill site, which suggest "severe nutrient limitations through the remainder of the Early Triassic, until returning to a highly productive continental margin in Middle Triassic time" (Grasby et al., 2019). Based on Mørk et al. (1999a)'s definition, the Deltadalen Member of the Vikinghøgda Formation encompasses the strata from the lithostratigraphic boundary at 88.08 m.b.s. up to the base of the Lusitaniadalen Member, which is interpreted to be located at 18.78 m.b.s. The increased frequency of storm-generated event-beds towards the top of the core may reflect an overall relative shallowing of the shelf, a real increase in storm frequency, an increase in storm intensity, or a combination of all three. The lack of independent palaeodepth indicators means that it is not possible to reject any options, although more proximal facies in the uppermost Induan at the Festningen section (Mørk et al., 1989) indicate overall shallowing of the shelf through the Induan in western Spitsbergen at least.

4.2. Conodont biostratigraphy

Of the three concretionary levels sampled for conodonts in the Deltadalen river profile, only the uppermost one (Concretion Level 3) yielded identifiable elements. The conodont elements are dark brown in colour, equivalent to conodont alteration index (CAI) of 2–3 (Fig. 4). A total of three Pa elements were identifiable and assigned to *H. parvus* (Kozur and Pjatakova, 1976). Diagnostic characters include their small size; a very large, slender, erect and slightly backward curved cusp; seven small denticles of similar size to each other, and are less than one-half the size of the cusp; and that the posterior part of the blade is steeply inclined (*cf.* Kozur, 1996). The FAD of *H. parvus* in Bed 27c at Meishan defines the base of the Triassic (Yin et al., 2001). This is the first record of *H. parvus* from Svalbard, which indicates that the PTB should be placed no higher than Concretionary Level 3 at this site. However, the conodont *H. parvus* is rare at this locality (fewer than one element per kg of rock), and so it is possible that the dissolution of additional rock may yield specimens from the underlying concretion levels.

4.3. U-Pb geochronology

The two analysed zircons from the tephra layer collected 2.49 m above the base of the Deltadalen River section just above the Concretion Level 3 (Fig. 4), are clear, euhedral, high-aspect ratio prisms with few inclusions. This tephra layer was correlated to a tephra sample at *ca.* 83.95 m.b.s. in the core, using key sandstone marker beds as well as the three concretion levels from the Deltadalen river section. They contain 14 and 2.5 pg of radiogenic Pb, respectively, resulting in relatively low precision analyses (Table 2). Analysis no. 1 is concordant, and analysis no. 2 is slightly reversely discordant, probably due to inaccurate correction for common Pb, reflecting the very low common/radiogenic Pb of the analysis. However, the ^{206}Pb/^{238}U-ages of the two analyses are identical within error giving a mean age of 252.13 ± 0.62 Ma (2σ, tracer uncertainties included; MSWD = 0.08) that is interpreted to approximate the age of deposition of the tephra
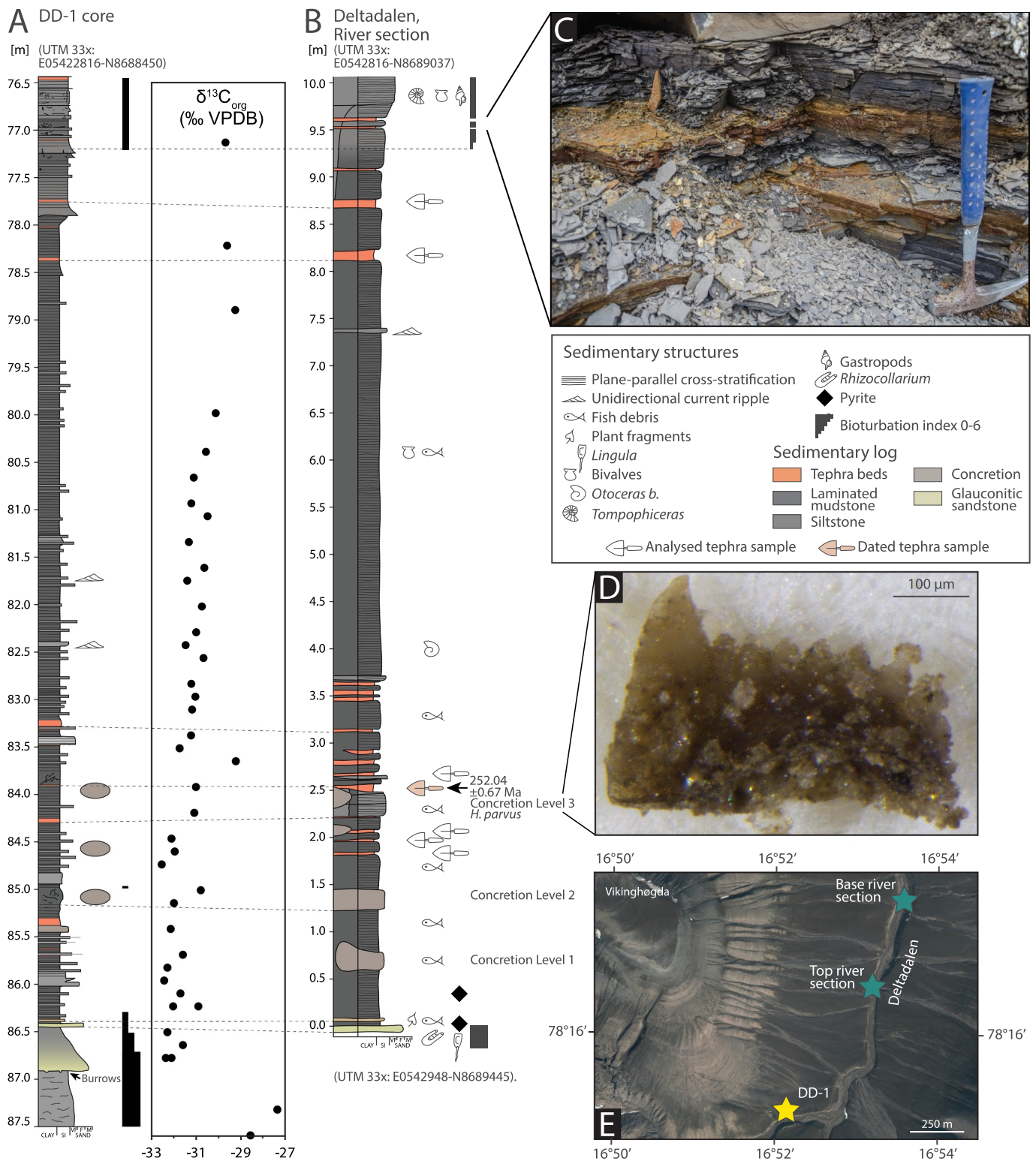
Fig. 4. Juxtaposition of the DD-1 core (A) and the Deltadalen river section (B) across the major facies change occurring at the base of the Vikinghøgda Formation and the 10 lowermost metres of the non-spiculitic mudstones. C) Weathered examples of tephra layer. D) *H. parvus* specimen found in CL 3. E) Aerial photograph displaying the location of the drill site and the Deltadalen river section. (For interpretation of the references to colour in this figure, the reader is referred to the web version of this article.)

bed. Although this age appears slightly older than the age of the PTB, it is overlapping and supports deposition of the tephra bed close to the PTB, also taking into consideration the possibility that the zircons represent antecrysts formed in a precursor magma chamber.

The differences between the tephra layers observed in the DD-1 core

and in the neighbouring Deltadalen river section (Fig. 4) are thought to be linked to varying lateral extents of the tephra beds as they might have been heterogeneously deposited on the seafloor. Due to their mm- to cm-scale thickness at the time of deposition, minor reworking episodes could have led to the segmentation of the tephra horizons. Note
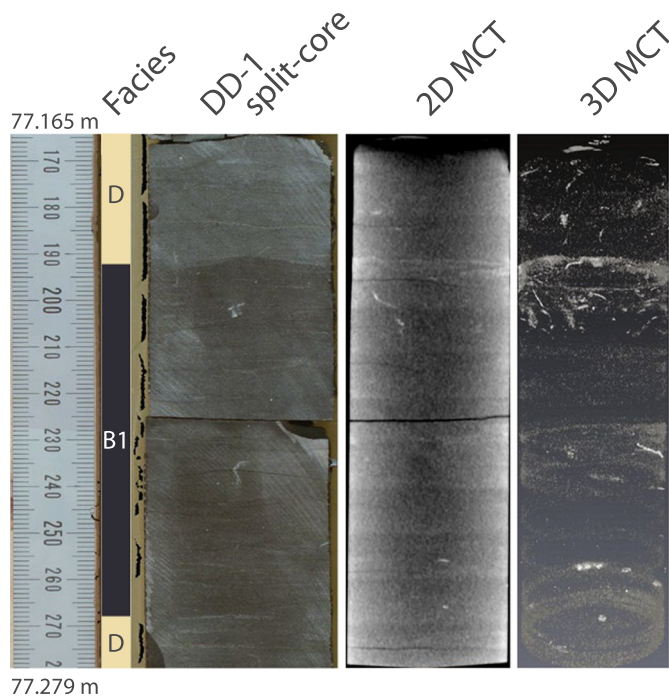
Fig. 5. Comparison of a core photograph, a 2D and a 3D micro-computed tomography (MCT) of the core interval located between 77.165 and 77.279 m.b.s. This illustrates the presence of very small and scattered bioturbations otherwise invisible to the naked eye, indicating that some small types of organism survived the EPME.

that a minor seafloor relief could have also generated micro-highs and lows, impacting on the sediment distribution in this low-energy setting.

4.4. Mineralogy and diagenesis

The Kapp Starostin Formation sandstone is green due to the presence of glauconite grains (Fig. 6). Deformation and fracturing of the glauconite grains is common and pyrite and apatite are present in fractures. It is unclear whether the apatite has an organic or inorganic origin. Moreover, the glauconite shows textures characteristic of partial dissolution and precipitation of calcite. The burial-related deformation also led to fragmentation of spicules in the rock. In addition to glauconite, the sandstone is dominated by detrital quartz grains and three generations of quartz cement (Fig. 6Div). The two last stages are characterised by euhedral crystals demonstrating high porosities during growth. Chlorite needles form bundles and partial coating locally, texturally related to the second and third stage of quartz cement. Calcite is locally filling the porosity and generally has a patchy occurrence.

The Vikinghøgda Formation siltstones are pyrite-bearing and contain moderate levels of TOC (0.2–2.0 wt%). Detrital grains include quartz, albite, K-feldspar, glauconite, tephra-fragments, and zircon. The K-feldspar is partially dissolved and replaced by calcite, but is also present as overgrowths on detrital K-feldspar. Calcite is locally pore-filling. Other authigenic minerals include chlorite, framboidal pyrite, and dolomite. The dolomite is commonly zoned, where outer rims are rich in iron and sometimes observed inter-grown with chlorite.

At least 27 tephra layers are identified based on core observations. They are commonly light grey to yellow-green in colour in the core and are well cemented, in contrast to where the same tephras are observed in outcrop (Figs. 2, 4, 6). The reason for the difference in character between tephras in core and outcrop is the high content of calcite in the tephras. During weathering, the calcite dissolves leading to tephra disintegration. In addition to the calcite, the main components of the tephras are fragments of volcanic rocks, chlorite, albite, and pyrite

(both framboidal and euhedral). The volcanic fragments are altered and characterised by tabular albite crystals, chlorite, and pyrite. The tephras with a greenish colour are rich in chlorite and poor in calcite. The nature of the volcanic fragments in the altered tephras is similar to the unaltered ones, showing textures that may be interpreted as former vesicles, now filled by framboidal pyrite and chlorite. Accessory minerals include rutile, K-feldspar, and chalcopyrite.

4.5. XRF results

This section will describe a selection of elemental concentrations and elemental ratios (Fig. 3). It includes Si/kcps, Zr/Rb, K/Ti, Fe/K, V/Cr, and Th/U (Table 3) ratios, as well as Pb and S elemental concentrations. Both U and Th values were obtained from XRF analysis targeted samples rather than from the core scan. A full XRF table of results is available as Supplementary material.

A high Si/kcps ratio indicates a high influence of detrital quartz and terrigenous, silica-rich material in the succession (Rothwell and Rack, 2006; Rothwell and Croudace, 2015). Zr/Rb reflects a grain size variation in the core (Dypvik and Harris, 2001), which can potentially be linked to changes in river runoff and hinterland precipitations (Rothwell and Croudace, 2015). Positive peaks indicate coarser material, potentially reflecting river floods or higher energy events such as storms or earthquake-induced tsunamis. Deviations in the K/Ti ratio generally reflects variations in sediment provenance: high K/Ti values reflect an acid (felsic) sources of terrigenous sediment, whereas low values would indicate a more basic (mafic) origin (Hodell et al., 2010; Rothwell and Croudace, 2015). A high Fe/K ratio is listed as indicative of higher continental precipitation leading to an increased water discharge and sedimentary input (Rothwell and Croudace, 2015). However, the presence of Ti-bearing minerals, notably in tephra layers, or pyrite, would strongly impact on such ratios. This would generate irrelevant peak artefacts and such climate proxies should therefore be considered with caution.

V/Cr and Th/U ratios are used as proxies for palaeo-oxygenation levels: increases in V/Cr and Th/U ratios simultaneously indicates a shift towards more anoxic conditions in the basin (Wignall and Twitchett, 1996). These two bimetal ratios were complemented with V and Cu-EF calculations in order to strengthen our interpretation of the palaeoredox conditions (*e.g.* Tribovillard et al., 2006; additional Zn, Ni, and Cr-EF calculations are available as Supplementary material), as some researchers have called the reliability of bimetal ratios alone into question (Algeo and Liu, in press). Variations in Pb concentrations potentially reflect periods of varying volcanically-driven coal fire intensity (Burger et al., 2019), which could have been ignited by the Siberian Traps intrusions (Svensen et al., 2009). Burger et al. (2019) also linked variations in S concentrations to volcanically-driven coal fires, although this needs to be considered with caution, as S is a redox- and pyritization-sensitive element.

4.5.1. XRF proxies in FA 1

In FA 1, the Si/kcps ratio parallels the Zr/Rb one. This parallel trend is also observed for the two Pb and S curves, whereas K/Ti and Fe/K's respective curves mirror each other. However, the glauconitic-sandstone-dominated FA 1 is subdivided in two subunits: the lower subunit covers the succession between the base of the core up to 89.95 m.b.s., while the upper subunit comprises the interval between 89.95 and 86.54 m.b.s (Fig. 3). In the lower subunit, each of the elemental ratios are generally characterised by longer oscillations wavelength and smaller oscillations amplitude in comparison to the upper subunit. Both Pb and S show a strong positive anomaly at *ca.* 92 m.b.s. While the average values of Si/kcps, Zr/Rb, Fe/K, Pb and S remain roughly constant in FA 1, the upper subunit is marked by a strong decrease in the K/Ti elemental ratio and a gradual increase in V/Cr (Fig. 3). Overall, the behaviour of these curves seems to be disconnected from the associated sedimentary Facies H1, H2, and H3.
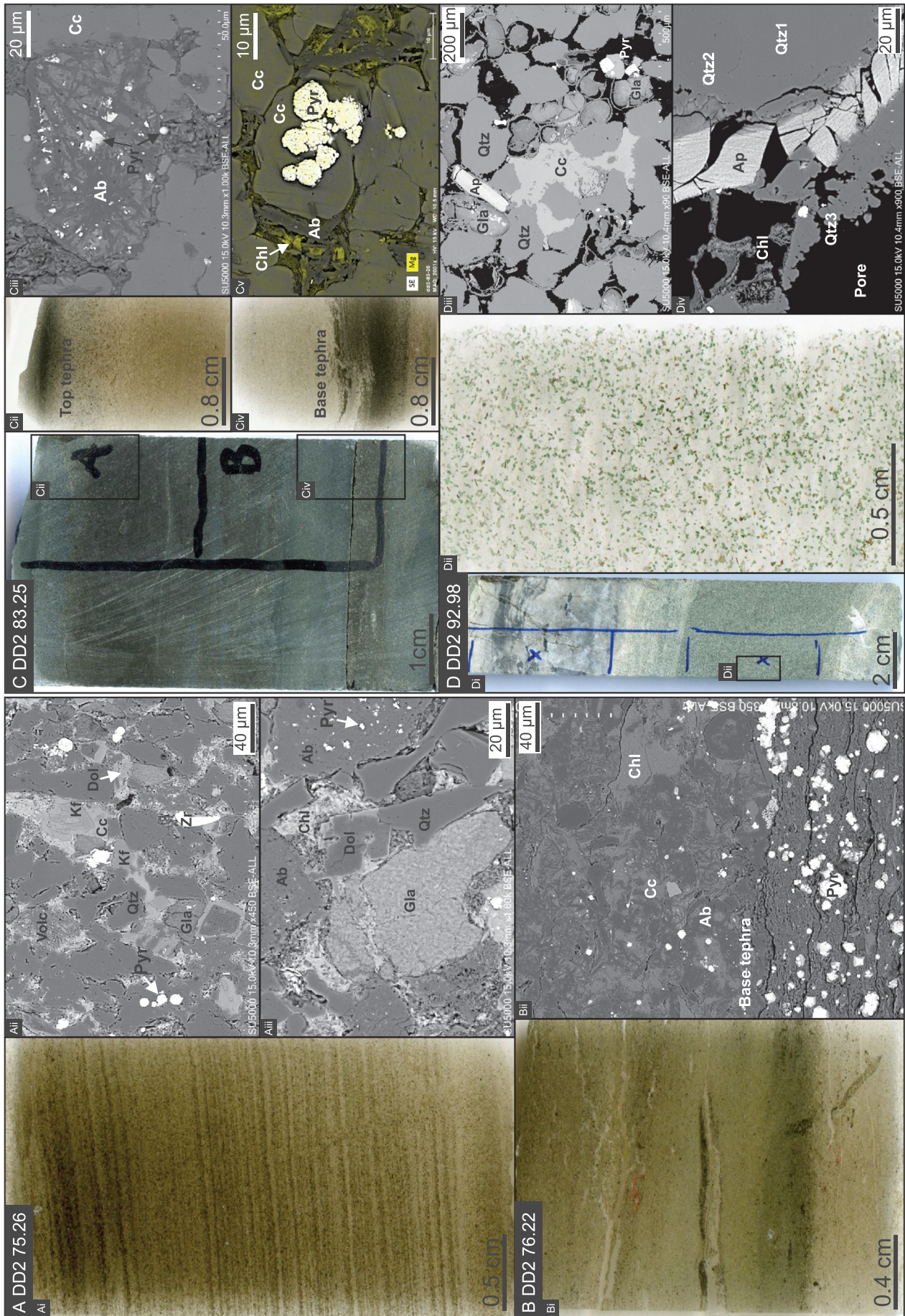
Fig. 6. Core photographs, and thin sections and SEM microphotographs of samples collected at A) 75.26 m.b.s., B) 76.22 m.b.s., C) 83.25 m.b.s., and D) 92.98 m.b.s. Ab: Albite; Ap: Apatite; Cc: calcite cement; Chl: Chlorite; Dol: Dolomite; Gla: Glauconite; Kf: K-Felspar; Pyr: Pyrite; Qtz: Quartz; Volc.: Volcaniclast; Zr: Zircon.

Table 1

Description and interpretation of the facies and facies associations recognised in the DD-1 core.

Facies	Description	Grain size	Interpretation	Facies Association	Lithostratigraphy
A	Grey bentonitic clay-size material. Note the orange weathering colour when exposed on outcrops.	Cl	Settlement of suspended tephra.		Vikinghøgda Fm., Deltadalen Mb.
B1	Finely laminated dark mudstone, Extremely rare visible bioturbation.	Cl - S, S <<< Cl	Deposition from suspended sediments, below the SWWB, deeper than Facies G: distal offshore (Bohacs et al., 2014; deepest interpreted facies).		Vikinghøgda Fm., Deltadalen Mb.
B2	Finely plane-parallel-laminated dark mudstone, with rare interbedded mm-scale laminae of s-vf-grained sandstone, rare bioturbations (less bioturbated than Facies B3).	Cl - S -VF, S << Cl	Deposition from suspended sediments, below the SWWB: distal- to middle offshore (Bohacs et al., 2014).		Vikinghøgda Fm., Deltadalen Mb.
B3	Finely plane-parallel-laminated dark mudstone, with isolated interbedded mm-scale laminae of s-vf-grained sandstone, potential reworking of glauconitic sandstone, scattered unidirectional current ripple-lamination, rare bioturbations, multiple occurrence of concreted horizons; pyrite content relatively high at first, decreasing up-core.	Cl - S -VF, S < Cl	Deposition from suspended sediments, at the contact of the SWWB: middle offshore (Bohacs et al., 2014).		Vikinghøgda Fm., Deltadalen Mb.
C1	Grey, parallel-laminated silt-/sandstone, with scattered interbedded laminae of s-vf-grained sandstone displaying cm-scale oscillation-ripples (Facies D), several episodes of intensive bioturbations between undisturbed intervals, sharp but conformable lower contact, arranged in fining-upward micro-sequences, note that the normal-grading is sharper in the lower part of the core than towards its top.	Cl - S -VF, S > Cl	Deposition from suspended sediments, at the contact of the SWWB: middle offshore to upper offshore (Bohacs et al., 2014), slightly shallower than Facies B3.	FA 2 - Storm-wave-dominated shelf covering the offshore to offshore transition domain, similar to Bohacs et al.'s (2014) FA1-S	Vikinghøgda Fm., Deltadalen Mb.
C2	Same as Facies C1, but with an increased sand-mud ratio, generally arranged in fining-upward intervals displaying an erosive lower contact; sporadic gradual transition from Facies C1 into C2 or between micro-sequences within C2, interbedded with event-beds (Facies D); episodes of bioturbation not as intense as in Facies C1.	Cl - S -VF, S >> Cl	Increased energy within the system compared to Facies C1, with an increased influence of storm-activity: upper o to offshore transition (Bohacs et al., 2014), slightly shallower than Facies C1.		Vikinghøgda Fm., Deltadalen Mb.
C3	Same as Facies C2, but with an increased sand-mud ratio, still arranged in fining-upward intervals but generally coarser-grained, massive or plane-parallel laminated, bioturbated intervals, interbedded with event-beds (Facies F).	Cl - S - VF - F, S >>> Cl	Increased energy within the system compared to Facies C2, with an increased influence of storm-activity: (offshore transition to) lower shoreface (Bohacs et al., 2014), slightly shallower than Facies C2.		Vikinghøgda Fm., Deltadalen Mb.
D	Grey, rippled- to HCS-cross-stratified sandstone, erosive to flat-sharp base, varying in thickness from 2 to 8 cm, sometimes amalgamated.	S - VF- F	Oscillatory-current or storm-influenced "event" beds.		Vikinghøgda Fm., Deltadalen Mb.
E	Cleaning- and coarsening-upward microsequences from vf-f-grained to f-grained sandstone, erosive lower-contact, reverse grading still visible despite the high degree of bioturbation; plane-parallel-laminated if not bioturbated, amalgamated.	VF - F	Sediment reworked by wave-triggered gravity flows accompanied by episodes of waxing flow, followed by subsequent wave erosion during rapidly waning flow conditions.		Vikinghøgda Fm., Deltadalen Mb.
F	Interfingering green glauconitic sandstone and plane parallel-laminated siltstone, fining-upwards into Facies B3.	S - VF	Deposition under diminishing energy conditions, with episodes of increased flow velocity reworking glauconitic substratum during a overal deepening of the system.	Transition between FA 1 and FA 2	Vikinghøgda Fm., Deltadalen Mb.
G	Dark grey to green, fining-upwards from vf-s-grained sandstone to siltstone, varying glauconite and chert content, thoroughly bioturbated by *Phycosyphoniform* and *Zoophycos*	S - VF - F	Depositional energy conditions decreasing upwards, within a well oxygenated environment and a low sedimentation rate.		Kapp Starostin Fm., Stensiöfjellet Mb.; Vikinghøgda Fm., Deltadalen Mb.
H1	Undisturbed, plane-parallel-laminated green glauconitic sandstone	F	Deposition under increased energy conditions, potentially corresponding to upper flow regime velocities within an upper shoreface to foreshore shoal environment, with a varying bioturbation intensity (mainly *Zoophycos* ?; Blomeier	FA 1 - Upper shoreface to foreshore deposits (Blomeier et al., 2013)	Kapp Starostin Fm., Stensiöfjellet Mb.
H2	Green glauconitic sandstone, varyingly silicified by chert nodules	F - M			Kapp Starostin Fm., Stensiöfjellet Mb.
H3	Thoroughly bioturbated, massive-looking green glauconitic sandstone, with occasional shell fragments (mainly *Zoophycos* ?)	F - M			Kapp Starostin Fm., Stensiöfjellet Mb.

4.5.2. XRF proxies in Facies F and the base of FA 2: from 86.54 to 77.30 m.b.s.

The fine sediments of Facies F and FA 2 record very distinct elemental ratios in comparison to the underlying, sandstone-dominated FA 1. Si/kcps and Zr/Rb values sharply decrease at the base of Facies F. While oscillations still occur in Facies B3, the curves stabilise towards their lowest recorded values in Facies B2 and B1 (Fig. 3). Facies F and B3 are characterised by stable yet oscillating K/Ti and V/Cr ratios (Fig. 3). In contrast, Facies B2 and B1 reflect very steady conditions as K/Ti and V/Cr stabilise, similar to Si/kcps and Zr/Rb (Fig. 3). However, K/Ti stabilises around values slightly higher in Facies B2 and B1 than in the underlying Facies F and B3, which contrasts with Si/kcps, Zr/Rb, and V/Cr elemental ratios. This period of quiescence in Facies B2 and B1 corresponds to the highest Th/U values recorded in the core (Fig. 3; Table 3).

The three Fe/K, Pb, and S curves display a trend which strongly contrasts with the one observed in FA 1, but they do not show the same stabilising trend seen in the other four elemental ratios. The Fe/K curve

Table 2
Summary of the U-Pb dating of zircon crystals.

Fraction no.	Th/U[a]	Pb*/Pb$_c$[b]	Pb$_c$ (pg)[b]	^{207}Pb/^{206}Pb[c]	% err[d]	^{207}Pb/^{235}U[c]	% err[d]	^{206}Pb/^{238}U[c]	% err[d]	Corr. coef.	^{207}Pb/^{206}Pb[e]	±[d]	^{207}Pb/^{235}U[e]	±[d]	^{206}Pb/^{238}U[e]	±[d]
1	0.281	17	0.84	0.05125	2.4	0.282	2.4	0.039860	0.55	0.116	252	54	252.0	5.3	252.0	1.3
2	1.023	2	1.08	0.04762	2.5	0.262	2.7	0.039893	0.28	0.576	81	60	236.2	5.6	252.17	0.68

[a] Model Th/U ratio iteratively calculated from the radiogenic ^{208}Pb/^{206}Pb ratio and ^{206}Pb/^{238}U age.

[b] Pb* and Pbc represent radiogenic and common Pb, respectively; mol% ^{206}Pb* with respect to radiogenic, blank and initial common Pb.

[c] Corrected for fractionation, spike, and common Pb; all common Pb was assumed to be procedural blank: ^{206}Pb/^{204}Pb = 18.07 ± 0.28%; ^{207}Pb/^{204}Pb = 15.57 ± 0.20%; ^{208}Pb/^{204}Pb = 37.85 ± 0.35% (all uncertainties 1-sigma).

[d] Errors are 2-sigma, propagated using the algorithms of Schmitz and Schoene (2007).

[e] Calculations are based on the decay constants of Jaffey et al. (1971). ^{206}Pb/^{238}U and ^{207}Pb/^{206}Pb ages corrected for initial disequilibrium in ^{230}Th/^{238}U using Th/U [magma] = 3.

is characterised by a sharp decrease at the base of Facies F, but its stabilisation towards low values, accompanied by diminishing oscillatory amplitudes, is gradual across the Facies B3 and B2 interval (Fig. 3). Similarly, Pb and S also show gradual stabilising trend across the entire Facies B interval. The Pb curve displays much stronger concentration variations in than in S, contrasting with the underlying FA 1, where S underwent much quicker and more important concentration variations.

4.5.3. XRF proxies in FA 2 between 77.30 m.b.s. and the top of the core

The interval between 77.30 m.b.s. and the top of the core is subdivided in four subunits (Fig. 3). The lowermost subunit encompasses the sediment between 77.30 and 43.22 m.b.s., and is characterised by oscillating elemental ratios and elemental concentrations. Notable sharp positive peaks in V/Cr occurs between 64.00 and 63.30 m.b.s., in the vicinity of two 0.5 cm-thick tephra layers, which were identified at 63.38 m.b.s., and strong Zr/Rb positive anomalies between 68 and 69 m.b.s. The second subunit covers the interval between 43.22 and 27.80 m.b.s. Its base corresponds to a sharp drop across all XRF curves (Fig. 3). Elemental ratios are more stable than the underlying unit, but sharp Zr/Rb and V/Cr peaks still occur. The third subunit ranges from 27.80 to 19.25 m.b.s. Each XRF curve in this interval display the most stable trend observed in any of the four subunits (Fig. 3). The uppermost subunit covers the interval between 19.25 m.b.s., nearly two metres below the base of the Lusitaniadalen Member of the Vikinghøgda Formation (located at 18.78 m.b.s), and the top of the core, in which elemental concentration and elemental ratios start to oscillate again (Fig. 3).

4.6. δ^{13}C and bulk organic matter properties of DD-1 core (Rock Eval, TOC)

The δ^{13}C values in the Stensiöfjellet Member of the Kapp Starostin and the lowermost metres of the Deltadalen Member of the Vikinghøgda Formation (FA 1) are between −26.9 and −29.1‰ (Fig. 3, Table 4). A sharp −4.9‰ CIE occurs at the top of FA 1,

reaching a minimum of −32.5‰, matching with a sharp V/Cr increase, while postdating the increased Pb concentration (Fig. 3). The δ^{13}C values recover from −31.3‰ at the base of Facies F to −30.9‰ at the top of Facies B2. The δ^{13}C values subsequently increase rapidly to −29.2‰ as the core grades into the laminated mudstone of Facies B1. The DD-1 δ^{13}C trend strongly resembles the one reported by Grasby et al.'s (2016) across the Kapp Starostin and the Vardebukta formations at Festningen (Fig. 7). However, the Festningen section recorded a far more gradual negative shift over *ca.* 4 m (Grasby et al., 2015), contrasting with the more condensed section recorded at the top of Facies G.

A second sharp 2–3‰ negative CIE occurs between 64.00 and 63.30 m.b.s., with a minimum value −31.1‰ at 63.35 m.b.s., 3 cm above two thin tephra layers (Fig. 3). This negative excursion matches with an increase in Fe/K, and V/Cr values, as well as increased Pb and S concentrations (Fig. 3). The δ^{13}C curve increases towards the highest values of DD-1 core, reaching −26.7‰ at 40.89 m.b.s. and −26.9‰ at 31.42 m.b.s. From 27.2‰ at 29.68 m.b.s., the δ^{13}C values diminish linearly to −29.9‰ at the top of the core, but values are more scattered in this uppermost interval than deeper in the core (Fig. 3). The onset of this negative shift 29.68 m.b.s. is interpreted as the base of the Olenekian (Payne et al., 2004; Burgess et al., 2014; Grasby et al., 2016; Foster et al., 2017a).

The total organic carbon content (TOC) varies between 0.1 and 2.5 wt% with lowest values (<0.2 wt%) in the Kapp Starostin Formation (Fig. 3). These values strongly increase between 89.00 and 78.00 m.b.s., following a change in lithology, where glauconitic sandstones are replaced by laminated mud and siltstones of Facies B3 and B2 (Fig. 3). Note that the drop of Pb concentration at 43.22 m.b.s. matches with a decrease of TOC. T$_{max}$ values are generally between 436 and 458 °C (mature), with the exception of some outliers at lower temperatures (<400 °C). Hydrogen Index (HI) is generally low, below 241 (Fig. 3). Comparing T$_{max}$ and HI results suggests that these HI values do not reflect the original HI of the rocks, as HI decreased with the increased maturity (Espitalié et al., 1977).

4.7. Evolutionary spectral analysis

The results of the five Si/kcps, Zr/Rb, K/Ti, Fe/K and V/Cr elemental ratios ESA analysis are displayed in Fig. 8. The three Zr/Rb, K/Ti and V/Cr curves display their strongest frequency peak at 0.04 cycles/m, implying that one cycle would measure *ca.* 25.1 m. Given that the measured interval is 54.25 m thick, it has therefore recorded 2.2 cycles. As it encompasses around 0.91 Myr, each of these major cycles is calculated to have lasted *ca.* 421 kyr (Fig. 8; Table 5). This suggests that these recorded signals reflect Milankovitch's long eccentricity cyclicity, which is thought to have lasted *ca.* 405 kyr during the Permian-Triassic transition (Li et al., 2016). The similarity between these three curves is limited to their major long eccentricity period, as

Table 3
U and Th concentration obtained through the XRF-analysis of targeted samples.

ICPMS sample	Sample depth (m)	U	Th	Th/U
DD-1_70.1	70.10	2.76	9.68	3.51
DD-1_72.76	72.76	2.37	8.90	3.76
DD-1_78.9	78.90	2.45	10.36	4.23
DD-1_79.28	79.28	2.68	10.87	4.06
DD-1_83.25	83.25	1.04	2.13	2.05
DD-1_84.49	84.49	1.16	1.88	1.63
DD-1_84.69	84.69	3.10	8.74	2.82
DD-1_90.08	90.08	0.36	1.01	2.80
DD-1_90.18	90.18	0.50	1.12	2.22
DD-1_94.42	94.42	2.80	3.94	1.40

Table 4
Summary table providing the results of geochemical analyses. It includes δ¹³C in per mil with respect to the Vienna Pee Dee Belemnite (VPDB), Total Organic Carbon (TOC), and Hydrogen Index (HI).

Depth (m)	$\delta^{13}C_{VPDB}$ (‰)	TOC (%)	HI (mg HC/g TOC)	Depth (m)	$\delta^{13}C_{VPDB}$ (‰)	TOC (%)	HI (mg HC/g TOC)	Depth (m)	$\delta^{13}C_{VPDB}$ (‰)	TOC (%)	HI (mg HC/g TOC)
10.61	−29.90	0.53	142	52.33	−28.13	0.64	199	79.85	−30.10	1.19	241
11.64	−31.24	0.65	193	52.67	−28.79	0.66	147	80.36	−30.51	1.39	214
12.67	−31.33	0.60	164	53.39	−28.45	0.53	179	80.56	−31.05	1.41	182
13.70	−29.87	0.47	152	54.05	−29.68	0.49	134	80.80	−31.17	1.39	173
14.59	−31.08	0.38	109	54.54	−28.53	0.75	206	81.06	−30.46	1.68	218
15.57	−28.44	0.29	125	55.50	−29.19	0.68	203	81.28	−31.28	1.78	171
16.78	−30.83	0.63	132	56.54	−29.42	0.57	171	81.58	−30.60	1.16	199
17.89	−29.11	0.60	180	56.82	−24.98	0.83	181	81.74	−31.35	2.51	185
18.24	−30.59	0.57	161	57.59	−29.47	0.85	199	82.00	−30.69	1.48	153
19.28	−29.66	0.38	114	58.85	−29.25	0.40	182	82.24	−30.95	1.46	217
19.76	−29.75	0.33	103	59.37	−29.76	0.70	180	82.41	−31.44	1.11	131
19.88	−28.33	0.37	114	59.62	−29.15	0.33	159	82.56	−30.62	0.82	166
20.83	−29.60	0.29	89	60.04	−30.28	0.67	170	82.56		0.88	78
21.46	−27.75	0.34	122	60.13	−30.32	0.45	148	82.71	−31.16	1.10	144
22.38	−29.21	0.47	68	60.23	−30.12	0.61	178	82.94	−31.01	1.23	137
23.24	−27.77	0.35	125	60.35	−29.78	1.01	181	83.10	−31.14	1.17	172
24.55	−29.42	0.45	140	60.47	−30.04	0.88	197	83.10		1.23	89
25.17	−27.98	0.37	104	60.61	−30.47	0.71	171	83.35	−31.16	0.59	119
26.37	−29.40	0.35	98	60.79	−30.51	0.49	152	83.50	−31.69	0.90	134
27.44	−27.43	0.23	97	60.88	−29.99	0.77	189	83.64	−29.21	0.49	135
28.57	−28.75	0.37	94	61.21	−30.31	0.50	139	83.60		0.54	76
29.68	−27.20	0.31	110	61.35	−30.42	0.41	139	83.82	−30.94	0.60	106
31.42	−26.87	0.27	92	61.81	−29.64	0.91	196	84.18	−31.03	0.81	138
32.27	−26.88	0.23	93	62.01	−30.43	0.86	217	84.36	−32.02	1.25	206
33.98	−26.87	0.36	122	62.10	−30.69	0.59	176	84.60	−31.88	0.68	115
34.60	−27.19	0.36	143	62.39	−30.81	0.98	146	84.71	−32.45	1.14	134
34.93	−27.43	0.36	75	62.79	−30.64	1.23	184	84.92	−30.72	0.97	178
35.48	−27.97	0.26	92	62.87	−29.85	0.60	172	85.13	−31.93	1.04	136
35.50		0.36	64	63.00	−30.48	0.73	177	85.43	−32.07	0.97	150
37.20	−28.15	0.22	84	63.25	−30.47	0.84	164	85.62	−31.53	0.87	178
37.98	−26.97	0.32	92	63.35	−31.07	0.69	114	85.71	−32.23	1.09	133
38.18	−27.63	0.26	87	63.40	−29.80	0.61	152	85.87	−32.37	1.10	126
38.40	−27.25	0.24	89	63.55	−29.77	0.41	124	86.00	−31.62	1.17	185
39.16	−27.68	0.33	85	63.64	−28.20	0.21	95	86.16	−31.95	0.47	97
40.00	−26.99	0.29	89	63.64	−29.01	0.19	120	86.25	−30.83	0.68	175
40.00		0.41	69	63.75	−29.87	0.37	126	86.40	−32.21	1.04	188
40.89	−26.65	0.42	118	63.94	−30.86	0.39	95	86.56	−31.52	0.65	161
41.30	−28.29	0.24	70	63.98	−29.84	0.46	134	86.22		0.81	109
41.88	−27.56	0.42	156	64.57	−28.93	0.44	83	86.59		0.85	140
42.20	−28.46	0.32	110	64.63		0.65	172	86.71	−32.02	0.70	78
42.59	−28.20	0.31	92	65.76	−28.84	0.28	98	86.79	−32.29	0.41	136
42.80	−27.59	0.26	104	66.51	−29.48	0.39	119	86.45		0.46	84
42.80		0.34	515	67.41	−29.83	0.47	68	87.26	−27.37	2.14	70
43.23	−28.60	0.59	123	67.69	−28.96	0.24	112	87.27		0.88	104
43.79	−27.64	0.66	167	68.76	−29.14	0.31	105	87.59	−28.54	0.46	68
43.80		0.83	123	69.31	−30.16	0.80	86	87.91	−27.73	0.87	93
44.31	−28.49	0.82	122	69.84	−28.58	0.23	78	88.67	−27.42	0.63	91
44.89	−28.44	0.58	178	70.71	−29.39	0.39	111	89.20	−28.01	0.30	30
45.50	−28.61	0.63	173	71.91	−28.88	0.24	88	90.86		0.18	22
46.50	−29.00	0.80	213	73.05	−28.90	0.22	78	90.86	−28.23	0.14	35
47.53	−28.39	0.63	191	73.81	−30.04	0.47	165	92.75	−29.08	0.14	43
48.95	−28.13	0.59	194	74.46	−29.41	0.42	107	93.52		0.19	207
49.86	−29.47	0.70	180	75.49	−29.47	0.69	137	95.88	−28.63	0.14	44
50.87	−28.67	0.85	229	77.10	−29.67	0.60	140	96.56		0.19	32
51.96	−29.32	0.75	182	78.13	−29.58	0.56	162	97.60	−26.87	0.51	47
52.10	−29.44	0.84	159	78.75	−29.23	1.03	194				

they do not share any other minor cyclical patterns. With cycles lasting 272.6, 171.7, and 87.4 kyr (Fig. 8; Table 5), the Zr/Rb curve does not seem to be associated with any Milankovitch-type of cyclicity other the 421 kyr long eccentricity, contrasting with the ESA-results of V/Cr. This elemental ratio's second strongest frequency peak corresponds to a 94.6 kyr period (Fig. 8; Table 5), potentially impacted by a 100 kyr short-eccentricity forcing (Li et al., 2016). The three last peaks observed in the V/Cr ESA spectrogram are associated with a 231.6, a 45.5, and 34.6 kyr cyclicity. This last value of 34.6 kyr is in the error range of Waltham's (2015) Earth axis obliquity period of 36.3 ± 2.6 kyr.

The cyclicity values associated with Si/kcps are 50.65, 379.23, 252.82, 182.03, and 59.10 kyr, listed in a descending power value

(Fig. 8; Table 5). Although these cycles do not have durations corresponding perfectly to the expected astronomical cycles, the 379.23 kyr periodicity is close to the values for long eccentricity. Only the shortest peaks of Fe/K ESA give periodicity values somewhat close to Milankovitch-type cyclical forcing (Waltham, 2015) with values of 39.2 (obliquity) and 27.9 (Earth axis precession), whereas the four strongest cyclical signals do not seem to be associated with any type of Milankovitch-type cyclical forcing (Fig. 8; Table 5).
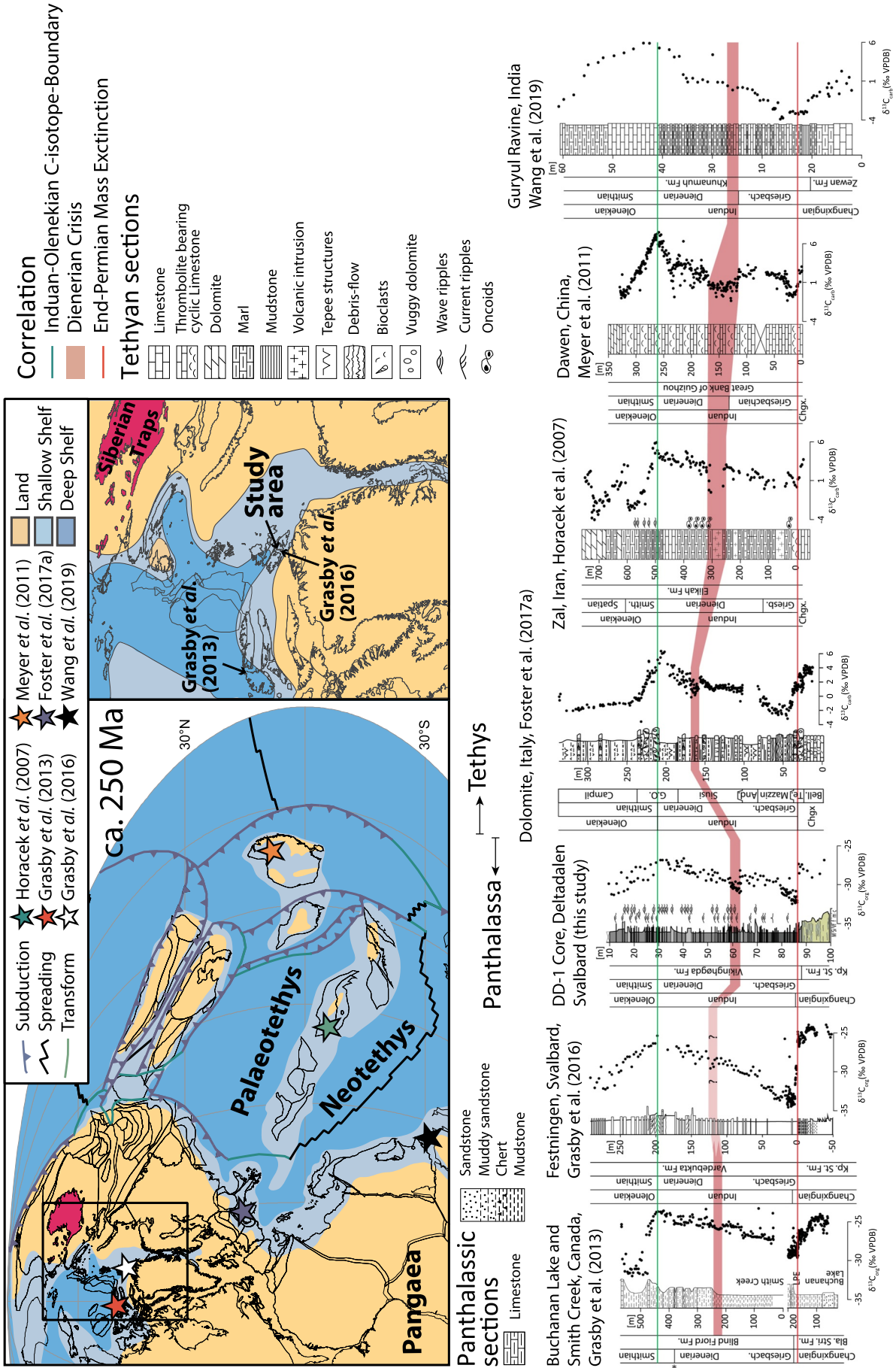
(caption on next page)

Fig. 7. Palaeogeographical map and correlation of Panthalassic (Grasby et al., 2013, 2016, this study) and Tethyan PTB sections (Horacek et al., 2007; Meyer et al., 2011; Foster et al., 2017a; Wang et al., 2019) flattened on the EPME (red line) and the C-isotope-Induan-Olenekian boundary (green line, after Burgess et al., 2014), highlighting the global significance of the Dienerian crisis (red area). Note that the Induan-Olenekian Boundary in the Smith Creek Section (Grasby et al., 2013), marked by an asterisk, is based on ammonoid biostratigraphy (after Tozer, 1965). (For interpretation of the references to colour in this figure legend, the reader is referred to the web version of this article.)

◂

5. Discussion

5.1. Sedimentation rate in Svalbard, and the Boreal Ocean

The Kapp Starostin Formation measures 320 m thickness in western Spitsbergen (Mørk et al., 1999a). Despite remaining uncertainties with respect to its age, it appears that this ramp system started developing during the Kungurian (*ca.* 283.5–273 Ma; Blomeier et al., 2013), and its uppermost strata are of Changhsingian age (*ca.* 252 Ma; Blomeier et al., 2013; Grasby et al., 2016). Therefore, the Kapp Starostin Formation potentially encompasses a time span of 32.5 to 21 Myr, which implies that, on average, 10 to 15 m of sediments accumulated every million years.

The Induan interval in Svalbard corresponds to a *ca.* 54.40 m thick package in Deltadalen, between base of Concretion Level 3 that yielded *H. parvus* at 84.10 m.b.s. and the base of the Olenekian at *ca.* 29.70 m.b.s., or *ca.* 54.25 m between the dated tephra bed at 83.95 m.b.s. and the base of the Olenekian, which is hereby defined by the carbon isotope record (Fig. 3). It implies that the boundary base of the Olenekian now lies *ca.* 13 m below the lithostratigraphic boundary between the Deltadalen and the Lusitaniadalen members of the Vikinghøgda Formation, where it was initially placed by Mørk et al. (1999b). The same time interval is *ca.* 200 m thick at Vardebukta in Festningen, western Spitsbergen (Figs. 1 and 7), suggesting that the PTB lies within the lowermost 5.60 m of Vardebukta Formation's non-spiculitic mudstones.

Based on our zircon age and Burgess et al.'s (2014) Induan-Olenekian boundary age, the Induan interval is interpreted to have lasted around 0.91 Myr. Average linear sedimentation rates during the Induan were therefore 61 m/Myr in central Spitsbergen and nearly four times faster, at 220 m/Myr in western Spitsbergen. Although these values are approximate and rely on the limited bio- and chronostratigraphical constraints in the core, they demonstrate that linear sedimentation rates in Svalbard were between 4 and 20 times faster in the Induan than in the Permian. A similar dramatic increase in linear sedimentation rates across the PTB has been previously documented in many locations worldwide, and is interpreted to have been a response to environmental changes at the time (Algeo and Twitchett, 2010). The magnitude of linear sedimentation rates recorded by the Induan strata of Svalbard, and the difference in rate between the Permian and Induan, are within the ranges recorded in Permian-Triassic marine shelf sections elsewhere in the world (Algeo and Twitchett, 2010).

High linear sedimentation rates in the Induan are recorded in shelf settings worldwide, but not in oceanic islands or offshore highs, and reflect increased chemical weathering, soil erosion and runoff in a hothouse climate, in locations with sufficient accommodation space to preserve the expanded sedimentary record (Algeo and Twitchett, 2010). Induan aquatic systems would have been very turbid environments, and such turbid conditions would have impacted the marine benthos.

5.2. Permian-Triassic boundary in Svalbard

The discovery of *H. parvus* in the Deltadalen river section is the first ever documented specimen in Svalbard, and it places the PTB *sensu* Yin et al. (2001) about 4.10 m above the base of the Vikinghøgda Formation at 84.00 m.b.s., and 2.30 m above the base of FA 2, within Vigran et al.'s (2014) *Reduviasporonites chalastus* Assemblage Zone. This is close to, but slightly lower than, Nakrem et al.'s (2008) prediction, based on assemblages of conodonts from higher in the section, that the

PTB should be between about 5 and 11 m above the base of the formation. Three specimens of *H. parvus* were found in Concretion Level 3 of the Deltadalen river section (Fig. 4), after dissolution of *ca.* 25 kg of rock. To date, the two underlying concretion levels have not yielded any conodonts, despite similar lithologies and similar masses of rock being dissolved, but we cannot exclude the possibility that *H. parvus* is present, but much rarer, in those horizons and so the current position of the PTB may need to be revised in the future.

The two 252.13 ± 0.62 Ma zircon crystals which were collected just above the *H. parvus*-bearing Concretion Level 3 (CL3) further confirm a near-PTB age for these deposits. They most probably originated from erupted Siberian Traps material given the lack of known proximal plate boundaries at the time (Fig. 7). Increasing the robustness of this dating, as well as diminishing its error margin will however require further data points.

At the PTB-GSSP in Meishan, the $\delta^{13}C$ values begin to drop prior to the extinction (Cao et al., 2009) which lies in Bed 24e (Wang et al., 2014), while the FAD of *H. parvus* occurring stratigraphically higher in Bed 27c (Yin et al., 2001). In the DD-1 core the same relative stratigraphic positions are recorded, with the shift towards more negative $\delta^{13}C$ values recorded between 87.26 and 86.79 m.b.s., and *H. parvus* recorded 2.8 m higher (Figs. 3 and 4). The same relative positions have been recorded in other locations elsewhere in the Arctic. In East Greenland, the negative CIE occurs in the uppermost 1–2 m of the Schuchert Dal Formation (Mettam et al., 2017), followed by collapse of marine and terrestrial ecosystems (the EPME) in the transition to the Wordie Creek Formation mudstones, with *H. parvus* being recorded some 23.5 m higher (Twitchett et al., 2001). Similarly, in Canada, Henderson and Baud (1997) and Beauchamp et al. (2009) documented the FAD of *H. parvus* 31.75 m above the base of the silty mudstones of the Blind Fiord Formation in the Canadian Arctic. Thus, the Deltadalen relative record of these key events (the CIE, EPME and FAD of *H. parvus*) corresponds with the GSSP in Meishan and other sites in the Arctic. Therefore, by definition, the uppermost strata of the Kapp Starostin Formation and the lowermost beds of the Vikinghøgda Formation are of Changhsingian age, which will require for these two formations' age to be formally updated.

Recent geochronology of the Meishan GSSP has dated the peak negative CIE at 251.950 ± 0.042 and the FAD of *H. parvus* at 251.902 ± 0.024 Ma (Burgess et al., 2014). In comparison to the <20 cm that this 50 kyr interval represents at Meishan (Yin et al., 2001), the 2.8 m interval of continuous sedimentation between the recorded extinction event and the FAD of *H. parvus* at Deltadalen represents *ca.* 45 kyr, based on calculated sedimentation rate.

Ammonoids have also been used to determine the position of the PTB at localities in Spitsbergen, especially in field studies (*e.g.* Mørk et al., 1999a; Nabbefeld et al., 2010; Foster et al., 2017b). At Deltadalen, the lowest *in situ Otoceras* occur at *ca.* 4 m and the lowest *Tompophiceras* at *ca.* 11.50 m above the base of the Deltadalen river section (Fig. 4). This suggests that, in Svalbard, *Otoceras* is a Triassic ammonoid. Similarly to East Greenland (Twitchett et al., 2001), conodonts re-appear before the first Induan age ammonoids in Deltadalen. It is likely that the sequence of relative re-appearance of these key biostratigraphically useful fossils is the same at other locations in Spitsbergen. To date, *H. parvus* has not yet been recorded from other central Spitsbergen locations such as Lusitaniadalen (Foster et al., 2017b). Based on our results, this is predicted to occur in the cemented concretions between 2 and 4.5 m above the base of the Vikinghøgda Formation at that location. At the Festningen section, western
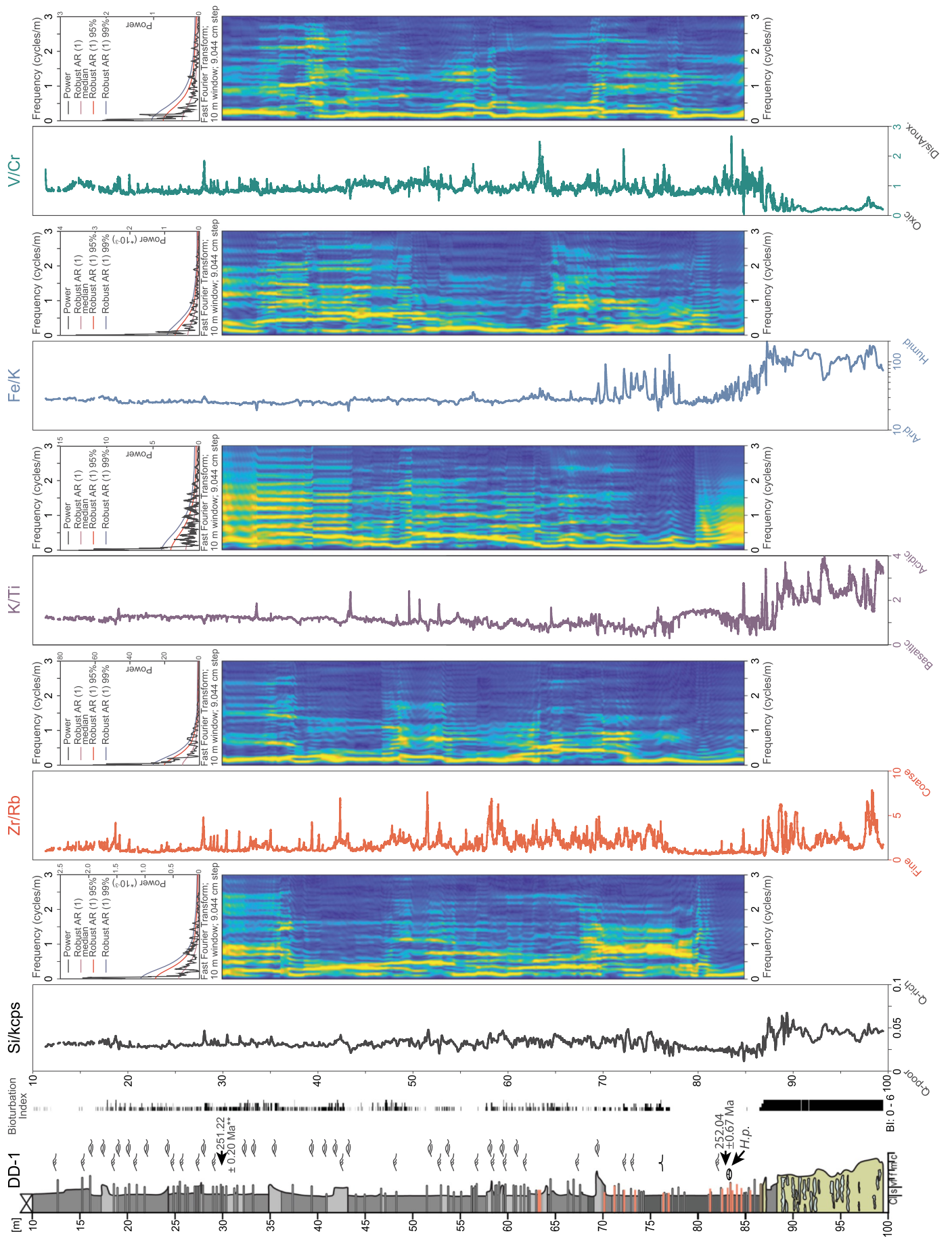
(caption on next page)

Fig. 8. DD-1 sedimentary log, bioturbation index, and ESA spectrograms accompanied by 2π MTM power spectrum, used to identify the wavelength of the major recognised cycles (see Table 5 for exact numbers) for each of the selected XRF elemental ratios.

Table 5
Summary table of the cyclicity recognised after analysing the 2π Multi-Taper Method (MTM) power spectrum plots and associated Evolutionary Spectral Analysis (ESA) spectrograms of selected XRF-elemental ratios for the interval comprised between comprised between the tephra bed (U-Pb age) and the Induan-Olenekian Boundary (251.22 ± 0.20 Ma, Burgess et al., 2014).

Elemental Ratio	Frequency peak (cycles/m)*	Cycle wavelength (m)	Number of cycles in the core	Duration of each cycles (Ky)	Associated cyclicity**
Si/Kcps	0.03	30.68	1.77	514.69	
	0.04	23.01	2.36	386.01	Eccentricity?
	0.07	15.34	3.54	257.34	
	0.09	11.05	4.91	185.29	
	0.28	3.59	15.13	60.16	
	0.16	6.28	8.64	105.28	Short eccentricity?
Zr/Rb	0.04	25.10	2.16	421.03	Long eccentricity
	0.06	16.24	3.34	272.41	
	0.10	10.23	5.30	171.60	
	0.19	5.21	10.41	87.39	
K/Ti	0.04	25.10	2.16	421.11	Long eccentricity
	0.06	16.24	3.34	272.48	
	0.08	12.01	4.52	201.40	
	0.32	3.17	17.09	53.24	
Fe/K	0.03	34.52	1.57	579.02	
	0.11	9.52	5.70	159.75	
	0.29	3.41	15.91	57.19	
	0.20	5.02	10.81	84.21	
	0.42	2.38	22.79	39.93	Obliquity?
	0.59	1.69	32.02	28.42	Earth axis precess.?
V/Cr	0.04	25.10	2.16	421.03	Long eccentricity
	0.18	5.64	9.62	94.61	Short eccentricity?
	0.07	13.80	3.93	231.48	
	0.37	2.71	20.02	45.46	
	0.49	2.06	26.33	34.55	Obliquity?

Measured interval: 54.25 m
Time encompassed in the analysis: 0.91 Ma
* Ordered by spectrum peak amplitude
** Based on Waltham (2015), and Li et al. (2016)

Spitsbergen, the lowest *in situ* ammonoids (*Tompophiceras*) are recorded 5.6 m above the base of the Vardebukta Formation (RJT pers. obs., 2015; identification by Dr. Al McGowan), and so it is predicted that the PTB, and the first *H. parvus*, if present, will be below that level.

5.3. Environmental proxies across the Permian-Triassic boundary

The geochemical fingerprinting of the tephras in the Deltadalen cores and outcrop is inhibited by their high alteration state, thus a Siberian Traps origin of the tephras cannot be demonstrated. However, based on palaeogeography and the U-Pb age of the tephras, together with the presence of *H. parvus* in the concretion level 3 (Fig. 3; Table 2), the deposition of lowermost part of the Vikinghøgda Formation occurred as the Siberian Traps LIP was active. It is therefore reasonable to suppose that the Siberian Traps is a plausible source for these layers.

Changes in Pb (and potentially S) concentrations within the core begin below the onset dysoxia or anoxia (Fig. 3), further supporting a link to the Siberian Traps: Burger et al. (2019) suggested that Pb concentrations increased around the extinction and PTB, potentially due to large amounts of coal burning as the Siberian Traps were erupting, although this has never been documented from outcrops or core in East Siberia. In any case, the emplacement of basaltic sills in carbonate-rich and organic carbon-bearing strata, including coal, (Ogden and Sleep, 2012; Svensen et al., 2018) led to contact metamorphism and the release of sediment-derived volatiles (Svensen et al., 2018). The DD-1 core records strong increases in the concentrations of Pb and S at the base of the Vikinghøgda Formation, associated with the large negative $\delta^{13}C$ excursion (Fig. 3). A similar trend was reported from the western coastline of Pangaea (Burger et al., 2019), although it is worth noting

that the disturbance in Pb and S concentrations in the core started prior to the $\delta^{13}C$ negative excursion (Fig. 3). Contact metamorphism associated with sill emplacements was a major source of the carbon release from the Siberian Traps, in addition to the mantle-derived carbon. The magnitude of global warming across the extinction event is *ca.* 7 °C (Kidder and Worsley, 2004; Svensen et al., 2009; Stordal et al., 2017; Burger et al., 2019), and potentially up to 9–12 °C inferred from oxygen-isotope analyses of brachiopods (Kearsey et al., 2009) and conodonts (Joachimski et al., 2012, 2020; Schobben et al., 2014; Chen et al., 2016).

Currently there are no good empirical estimates of Permian-Triassic palaeotemperature change for sites in or around Svalbard. Oxygen isotope data from P-Tr brachiopod shells from Spitsbergen published by Gruszczynski et al. (1989), were very likely to be diagenetically altered (Mii et al., 1997), and so unreliable for palaeotemperature estimates. Even if the data were adequate, caution would be needed in their interpretation due to the possible changes in salinity. In their study of an East Greenland locality, van Soelen et al. (2018) provided evidence from acritarch morphology that seawater salinity may have been reduced in shelf settings due to changes in the hydrological cycle and elevated riverine input. In contrast, Heindel et al. (2018) reported halophilic biomarkers indicative of hypersaline episodes closer to the equator. If applicable elsewhere, as modelled by Kidder and Worsley (2004), this would mean that temperature estimates from oxygen isotope analyses would provide temperature estimates that are too high. But the rate at which these temperature variations occurred remained underestimated (Kemp et al., 2015). Nevertheless, the East Greenland section was a narrow seaway which may explain the freshwater signature, it is not necessarily reflective of more open water records such

as those of Svalbard.

Variations of the global and regional precipitation regime associated with Permian-Triassic global warming are poorly documented. Atmospheric CO_2 concentrations are typically assumed to have reached *ca.* 3000 ppmv (*e.g.* Kidder and Worsley, 2004), but proxy evidence from stomatal index data suggest that atmospheric CO_2 rose from 558 to 1369 ppmv in the early to middle Changhsingian, to 4024 ppmv in the latest Changhsingian, before culminating in values of 7243 ppmv in the earliest Induan (Retallack and Jahren, 2008). Such an increased atmospheric CO_2 concentration is predicted to have led to a polarward expansion of the Hadley Cell and its associated arid climate belt (Kidder and Worsley, 2004; Woods, 2005). However, the atmospheric system's response is complex and linked to other parameters, including ozone depletion and warming sea surface temperatures (Sanchez-Lorenzo et al., 2017; Staten et al., 2018; Chemke and Polvani, 2019). The XRF data from the DD-1 core supports this polarward expansion of the Hadley Cell, with a reduction in Fe/K values across the PTB (Fig. 3), suggesting more arid climatic conditions over the study area (Rothwell and Croudace, 2015). This change towards more arid conditions was accompanied by the replacement of the more felsic, Permian source of sediments by a more basaltic one, as testified by a drop in K/Ti values (Fig. 3). Such an increase in aridity during the Permian-Triassic transition and into the Early Triassic was also reported from the Karoo Basin, located at the time in the interior of Pangaea at *ca.* 60°S (Smith and Botha-Brink, 2014; MacLeod et al., 2017; Viglietti et al., 2018). This documented increase in aridity seems to be in contradiction with the dramatic increase in sedimentation rate observed during the Induan, accompanied by the palynological shift documented in the northern margins of Pangaea across of the PTB interval, which certainly suggest an increase in continental runoff in these areas (Mettam et al., 2017; van Soelen et al., 2018). Nevertheless, a possibly lesser-vegetated landscape due to increased aridity (Benton et al., 2004) during the Early Triassic, combined with a potential increase in seasonal precipitation (Gautam, 2018), may be ideal conditions to facilitate increased weathering and denudation of material to the oceans.

One of the most significant environmental changes recorded in marine settings worldwide is a reduction in the concentration of dissolved oxygen, and the appearance and widespread development of dysoxic and anoxic 'dead zones' (*e.g.* Wignall and Twitchett, 1996; Lau et al., 2016). In Deltadalen, this is shown macroscopically by the change in facies from thoroughly bioturbated to laminated, and chemically by an increase in V/Cr in Th/U values (Fig. 3). In FA 2, these periods of low oxygen levels also display EF-values >1. This change from oxic to dysoxic/anoxic conditions also occurred at shallower depths, closer to the palaeo-coastline (Vardebukta, Festningen section; Wignall et al., 2016), although Beatty et al. (2008) and Proemse et al. (2013) documented pockets of well-oxygenated shallow-marine waters in the Sverdrup Basin. The V/Cr data suggests that oxygen availability began to decline prior to the extinction event (Fig. 3). This is also shown by organic geochemical data from Lusitaniadalen (Nabbefeld et al., 2010). At the same time, oscillations in the elemental ratios of Si/kcps, Zr/Rb, K/Ti, and Fe/K, begin to increase in amplitude (Fig. 3). If the Pb and S concentration increases at *ca.* 92 m.b.s. are related to the Siberian Traps (Fielding et al., 2019; Joachimski et al., 2020), it would imply that the climatic and redox disturbances in both the atmosphere and the oceans were delayed, before exponentially increasing from 89.95 m.b.s., as suggested by Dustira et al. (2013) and Grasby et al. (2015). This could mark the onset of the primary extrusive phase of the LIP (Fielding et al., 2019; Joachimski et al., 2019), up until the major eruption episode(s) and sill emplacement of the Siberian Traps at 86.89 m.b.s. Consequently, the extinction interval is synchronous with the main pulse of sill intrusions and a quiescence in eruptive activity (Burgess and Bowring, 2015; Burgess et al., 2017).

5.4. Induan cyclicity

In the interval from the U-Pb-dated tephra bed at 83.95 m.b.s. to the base Olenekian carbon isotope change at *ca.* 29.70 m.b.s., the elemental ratios Zr/Rb, K/Ti, and V/Cr all show robust cyclicity in the long eccentricity (400 kyr) band (Fig. 8; Table 5). However, only a little more than two cycles are recorded in this interval. Short eccentricity, obliquity, and precession cycles are found only for some element ratios and together with periodicities that cannot be explained by astronomical forcing (Table 5). We therefore consider only the *ca.* 400 kyr period to be well supported by the data. This cycle is considered the most likely astronomical cycle to be observed in strata older than the Caenozoic, and is the cycle most commonly used for Mesozoic and Palaeozoic cyclostratigraphy (*e.g.* Laskar et al., 2011; Waltham, 2015; Li et al., 2016).

Contrasting with these results and the *ca.* 0.9 Myr duration of this stage used herein based on Burgess et al. (2014) data, Li et al. (2016) proposed that the Induan in South China spanned 2 Myr, recording five 405 kyr cycles. The question of a short-duration or long-duration Induan is still unresolved; for a recent review of this controversy see Huang (2018).

5.5. Dienerian crisis

Shortly after initial recovery of benthic biota at 74.00 m.b.s., the core data record another environmental crisis that was associated with reduced levels of oxygen in the water column. This crisis is evidenced by the sharp, 2–3‰ negative $\delta^{13}C$ excursion, concomitant with an increase in TOC values, between 64.00 and 63.30 m.b.s., and sharp positive peaks in V/Cr (Fig. 3). This negative CIE is herein correlated to a CIE of similar magnitude that has been recorded in upper Induan (Dienerian) strata of the low-palaeolatitude Werfen Formation, northern Italy, by Foster et al. (2017a), and which also coincides with a drop in benthic diversity (Foster et al., 2017a). The same benthic crisis has also been documented in the fossil record of the western US, which, at the time, was located at low palaeolatitudes (15–20°N), on the eastern margin of Panthalassa (Ware et al., 2011; Hofmann et al., 2013, 2014, 2015).

In addition to being recorded in northern Italy (Foster et al., 2017a) and from the DD-1 core (Fig. 7), a similar negative CIE has been recorded in the same stratigraphic position at Festningen in western Spitsbergen (Grasby et al., 2016), Zal in Iran (Horacek et al., 2007), Dawen in China (Meyer et al., 2011), the Guryul Ravine in India (Wang et al., 2019), and in the Canadian Arctic (Grasby et al., 2013). Our new data and these additional records support the hypothesis that the Dienerian crisis was a global event that impacted marine recovery during the Early Triassic (Foster et al., 2017a). Reduced water-column oxygenation (Fig. 3) could be linked to slower ocean circulation (*cf.* Foster et al., 2017a) and/or a reduction in dissolved oxygen concentration associated with a brief warming event or eutrophication. The proximity of the $\delta^{13}C$ negative shift to two thin tephra layers in the DD-1 core suggest a possible link between the Dienerian crisis and a discrete episode of volcanic activity.

6. Conclusions

The drilling operation conducted in Deltadalen, central Spitsbergen, resulted in a near-complete recovery of two >90 m cores spanning the PTB and encompassing the entire Induan. Data from these two cores were complemented by the collection of samples from the Deltadalen river section outcrops. The two cores consist of *ca.* 15 m of Upper Permian, green, bioturbated, glauconitic sandstone with common chert-rich intervals belonging to the Kapp Starostin Formation at their base. This glauconitic sandstone was deposited in an upper shoreface to foreshore environment on the northern margin of Pangaea. The remainder of the cores record the overlying Upper Permian to Lower

Triassic, non-spiculitic, offshore shelfal mudstones of the lower Vikinghøgda Formation. Study of the cores and associated outcrop samples have revealed:

1. The PTB is located about 4 m above the base of the Vikingøgda Formation, within Vigran et al. (2014)'s *Reduviasporonites chalastus* Assemblage Zone, following the discovery of the conodont *Hindeodus parvus* in the river section of Deltadalen.

2. The concretion horizon that yielded *H. parvus* lies just below a tephra bed that has been dated at 252.13 ± 0.62 Ma, which is within error of the PTB GSSP. Additional zircons would be needed to further refine this age. The local FAD of *H. parvus* and the tephra bed occurs *ca.* 2.50 m above the extinction event, recorded locally by the loss of bioturbation, and its associated sharp negative excursion in $\delta^{13}C$ values.

3. Linear sedimentation rates based on preserved rock thicknesses dramatically increased during the Induan in Spitsbergen, and were 4 to 20 times faster than during the Permian. The estimated sedimentation rates and the relative change across the PTB are within the ranges of published data from other shelf sections worldwide.

4. The elemental ratios Zr/Rb, K/Ti, and V/Cr record robust cyclicity in the long eccentricity (400 kyr) band. Just over two full cycles are preserved within the 54.25 m thick, 0.91 Myr Induan of the study site. Our data suggest that shorter cycles, possibly equivalent to eccentricity, obliquity and precession cycles, may be recorded by some element ratios, together with other periodicities that cannot be explained by astronomical forcing.

5. A $\delta^{13}C$ negative excursion documented between 64.00 and 63.30 mbs in DD-1 is interpreted to correspond to the 'Dienerian crisis' of Foster et al. (2017a, 2017b). In combination with recent publications, this further supports the hypothesis that the Dienerian crisis was a global event. Two thin tephra layers are recorded close to this CIE, suggesting that the crisis may have been triggered by volcanic activity.

Declaration of competing interest

The authors of this paper do not have any conflicts of interest to report.

Acknowledgments

Appendix A. Supplementary data

Supplementary data to this article can be found online at https://doi.org/10.1016/j.palaeo.2020.109732.

References

Algeo, T.J., Liu, J., 2020. A re-assessment of elemental proxies for paleoredox analysis. Chem. Geol. 119549.

Algeo, T.J., Twitchett, R.J., 2010. Anomalous Early Triassic sediment fluxes due to elevated weathering rates and their biological consequences. Geology 38 (11), 1023–1026.

Algeo, T., Henderson, C.M., Ellwood, B., Rowe, H., Elswick, E., Bates, S., Lyons, T., Hower, J.C., Smith, C., Maynard, B., Hays, L.E., 2012. Evidence for a diachronous Late Permian marine crisis from the Canadian Arctic region. GSA Bull. 124 (9–10), 1424–1448.

Ballo, E.G., Augland, L.E., Hammer, Ø., Svensen, H.H., 2019. A new age model for the Ordovician (Sandbian) K-bentonites in Oslo, Norway. Palaeogeogr. Palaeoclimatol. Palaeoecol. 520, 203–213.

Baresel, B., Bucher, H., Brosse, M., Cordey, F., Guodun, K., Schaltegger, U., 2017. Precise age for the Permian–Triassic boundary in South China from high-precision U-Pb geochronology and Bayesian age–depth modeling. Solid Earth 8 (2), 361–378.

Baud, A., 2014. The global marine Permian-Triassic boundary: over a century of adventures and controversies. Albertiana 42, 1–21.

Beatty, T.W., Zonneveld, J.P., Henderson, C.M., 2008. Anomalously diverse Early Triassic ichnofossil assemblages in northwest Pangea: a case for a shallow-marine habitable zone. Geology 36 (10), 771–774.

Beauchamp, B., Baud, A., 2002. Growth and demise of Permian biogenic chert along northwest Pangea: evidence for end-Permian collapse of thermohaline circulation. Palaeogeogr. Palaeoclimatol. Palaeoecol. 184 (1–2), 37–63.

Beauchamp, B., Henderson, C.M., Grasby, S.E., Gates, L.T., Beatty, T.W., Utting, J., Noel, P., James, N.P., 2009. Late Permian sedimentation in the Sverdrup Basin, Canadian Arctic: the Lindström and Black Stripe Formations. Bull. Can. Petrol. Geol. 57 (2), 167–191.

Benton, M.J., Tverdokhlebov, V.P., Surkov, M.V., 2004. Ecosystem remodelling among vertebrates at the Permian–Triassic boundary in Russia. Nature 432 (7013), 97–100.

Birkenmajer, K., 1977. Triassic sedimentary formations of the Hornsund area. Spitsbergen. Studia Geologica Polonica 51, 7–74.

Black, B.A., Lamarque, J.F., Shields, C.A., Elkins-Tanton, L.T., Kiehl, J.T., 2014. Acid rain and ozone depletion from pulsed Siberian Traps magmatism. Geology 42 (1), 67–70.

Blomeier, D., Dustira, A., Forke, H., Scheibner, C., 2011. Environmental change in the Early Permian of NE Svalbard: from a warm-water carbonate platform (Gipshuken Formation) to a temperate, mixed siliciclastic-carbonate ramp (Kapp Starostin Formation). Facies 57 (3), 493–523.

Blomeier, D., Dustira, A.M., Forke, H., Scheibner, C., 2013. Facies analysis and depositional environments d a storm-dominated, temperate to cold, mixed siliceous-carbonate ramp: the Permian Kapp Starostin Formation in NE Svalbard. Nor. J. Geol. 93, 75–93.

Bohacs, K.M., Lazar, O.R., Demko, T.M., 2014. Parasequence types in shelfal mudstone strata—Quantitative observations of lithofacies and stacking patterns, and conceptual link to modern depositional regimes. Geology 42 (2), 131–134.

Bond, D.P., Grasby, S.E., 2017. On the causes of mass extinctions. Palaeogeogr. Palaeoclimatol. Palaeoecol. 478, 3–29.

Botha, J., Huttenlocker, A.K., Smith, R.M., Prevec, R., Viglietti, P., Modesto, S.P., 2020. New geochemical and palaeontological data from the Permian-Triassic boundary in the South African Karoo Basin test the synchronicity of terrestrial and marine extinctions. Palaeogeogr. Palaeoclimatol. Palaeoecol. 540, 109467.

Buchan, S.H., Challinor, A., Harland, W.B., Parker, J.R., 1965. The Triassic stratigraphy of Svalbard. Nor. Polarinst. Skr. 135, 1–92.

Burger, B.J., Estrada, M.V., Gustin, M.S., 2019. What caused Earth's largest mass extinction event? New evidence from the Permian-Triassic boundary in northeastern Utah. Glob. Planet. Chang. 177, 81–100.

Burgess, S.D., Bowring, S.A., 2015. High-precision geochronology confirms voluminous magmatism before, during, and after Earth's most severe extinction. Sci. Adv. 1 (7), 1–14.

Burgess, S.D., Bowring, S., Shen, S.Z., 2014. High-precision timeline for Earth's most severe extinction. Proc. Natl. Acad. Sci. 111 (9), 3316–3321.

Burgess, S.D., Muirhead, J.D., Bowring, S.A., 2017. Initial pulse of Siberian Traps sills as the trigger of the end-Permian mass extinction. Nat. Commun. 8 (1), 164.

Cao, C., Love, G.D., Hays, L.E., Wang, W., Shen, S., Summons, R.E., 2009. Biogeochemical evidence for euxinic oceans and ecological disturbance presaging the end-Permian mass extinction event. Earth Planet. Sci. Lett. 281 (3–4), 188–201.

Catuneanu, O., Abreu, V., Bhattacharya, J.P., Blum, M.D., Dalrymple, R.W., Eriksson, P.G., ... Giles, K.A., 2009. Towards the standardization of sequence stratigraphy. Earth-Science Reviews 92 (1-2), 1–33.

Chemke, R., Polvani, L.M., 2019. Exploiting the abrupt $4\times$ CO2 scenario to elucidate tropical expansion mechanisms. J. Clim. 32 (3), 859–875.

Chen, J., Shen, S.Z., Li, X.H., Xu, Y.G., Joachimski, M.M., Bowring, S.A., Erwin, D.H., Yuan, D.X., Chen, B., Zhang, H., Wang, Y., Cao, C.Q., Zeng, Q.F., Mu, L., 2016. High-resolution SIMS oxygen isotope analysis on conodont apatite from South China and implications for the end-Permian mass extinction. Palaeogeogr. Palaeoclimatol. Palaeoecol. 448, 26–38.

Clarkson, M.O., Kasemann, S.A., Wood, R.A., Lenton, T.M., Daines, S.J., Richoz, S., Ohnemueller, F., Meixner, A., Poulton, S.W., Tipper, E.T., 2015. Ocean acidification and the Permo-Triassic mass extinction. Science 348 (6231), 229–232.

Cutbill, J.L., Challinor, A., 1965. Revision of the stratigraphical scheme for the Carboniferous and Permian rocks of Spitsbergen and Bjørnøya. Geol. Mag. 102 (5), 418–439.

Dallmann, W.K., 1999. Introduction. In: Dallmann, W.K. (Ed.), Lithostratigraphic Lexicon of Svalbard. Norsk Polarinstitutt, Tromsø, pp. 11–24.

Dallmann, W.K., Gjelberg, J.G., Harland, W.B., Johannessen, E.P., Keilen, H.B., Lønøy, A., Nilson, I., Worsley, D., 1999. Upper palaeozoic lithostratigraphy. In: Dallmann, W.K. (Ed.), Lithostratigraphic Lexicon of Svalbard. Norsk Polarinstitutt, Tromsø, pp. 25–126.

Dustira, A.M., Wignall, P.B., Joachimski, M., Blomeier, D., Hartkopf-Fröder, C., Bond, D.P., 2013. Gradual onset of anoxia across the Permian–Triassic boundary in Svalbard, Norway. Palaeogeogr. Palaeoclimatol. Palaeoecol. 374, 303–313.

Dypvik, H., Harris, N.B., 2001. Geochemical facies analysis of fine-grained siliciclastics using Th/U, Zr/Rb and (Zr+ Rb)/Sr ratios. Chem. Geol. 181 (1–4), 131–146.

Dypvik, H., Riber, L., Burca, F., Rüther, D., Jargvoll, D., Nagy, J., Jochmann, M., 2011. The Paleocene–Eocene thermal maximum (PETM) in Svalbard—clay mineral and geochemical signals. Palaeogeogr. Palaeoclimatol. Palaeoecol. 302 (3–4), 156–169.

Ehrenberg, S.N., Pickard, N.A.H., Henriksen, L.B., Svana, T.A., Gutteridge, P., Macdonald, D., 2001. A depositional and sequence stratigraphic model for cold-water, spiculitic strata based on the Kapp Starostin Formation (Permian) of Spitsbergen and equivalent deposits from the Barents Sea. AAPG Bull. 85 (12), 2061–2087.

Espitalié, J., Madec, M., Tissot, B., Menning, J.J., Leplat, P., 1977. Source rock characterization methods for petroleum exploration. In: Procedures of the 1977 Offshore Technology Conference. 3. pp. 439–443.

Fielding, C.R., Frank, T.D., McLoughlin, S., Vajda, V., Mays, C., Tevyaw, A.P., ... Crowley, J.L., 2019. Age and pattern of the southern high-latitude continental end-Permian extinction constrained by multiproxy analysis. Nature communications 10 (1), 385.

Foster, W.J., Danise, S., Price, G.D., Twitchett, R.J., 2017a. Subsequent biotic crises delayed marine recovery following the late Permian mass extinction event in northern Italy. PLoS One 12, e0172321. https://doi.org/10.1371/journal.pone.0172321.

Foster, W.J., Danise, S., Twitchett, R.J., 2017b. A silicified Early Triassic marine assemblage from Svalbard. J. Syst. Palaeontol. 15, 851–877.

Gautam, M.D., 2018. Simulation of Climate Across the Permian-Triassic Boundary With a Focus on Phytogeographical Data Analysis. Master's thesis. Department of Earth and Environmental Sciences, University of Texas at Arlington, USA, pp. 1–61.

Grasby, S.E., Beauchamp, B., 2008. Intrabasin variability of the carbon-isotope record across the Permian–Triassic transition, Sverdrup Basin, Arctic Canada. Chem. Geol. 253 (3–4), 141–150.

Grasby, S.E., Beauchamp, B., 2009. Latest Permian to Early Triassic basin-to-shelf anoxia in the Sverdrup Basin, Arctic Canada. Chem. Geol. 264 (1–4), 232–246.

Grasby, S.E., Beauchamp, B., Embry, A., Sanei, H., 2013. Recurrent Early Triassic ocean anoxia. Geology 41 (2), 175–178.

Grasby, S.E., Beauchamp, B., Bond, D.P., Wignall, P., Talavera, C., Galloway, J.M., ... Blomeier, D., 2015. Progressive environmental deterioration in northwestern Pangea leading to the latest Permian extinction. GSA Bulletin 127 (9-10), 1331–1347.

Grasby, S.E., Beauchamp, B., Bond, D.P., Wignall, P.B., Sanei, H., 2016. Mercury anomalies associated with three extinction events (Capitanian crisis, latest Permian extinction and the Smithian/Spathian extinction) in NW Pangea. Geol. Mag. 153 (2), 285–297.

Grasby, S.E., Them II, T.R., Chen, Z., Yin, R., Ardakani, O.H., 2019. Mercury as a proxy for volcanic emissions in the geologic record. Earth Sci. Rev. 102880.

Gruszczynski, M., Hałas, S., Hoffman, A., Małkowski, K., 1989. A brachiopod calcite record of the oceanic carbon and oxygen isotope shifts at the Permian/Triassic transition. Nature 337 (6202), 64.

Hammer, Ø., Jones, M.T., Schneebeli-Hermann, E., Hansen, B.B., Bucher, H., 2019. Are Early Triassic extinction events associated with mercury anomalies? A reassessment of the Smithian/Spathian boundary extinction. Earth Sci. Rev. 195, 179–190.

Harland, W.B., Geddes, I., 1997. The geology of Svalbard. In: Harland, W.B. (ed.). Geological Society, London, Memoirs 17 (1), 3–15.

Heindel, K., Foster, W.J., Richoz, S., Birgel, D., Roden, V.J., Baud, A., Brandner, R., Krystyn, L., Mohtat, T., Koşunk, E., Twitchett, R.J., Reitner, J., Peckmann, J., 2018. The formation of microbial-metazoan bioherms and biostromes following the latest Permian mass extinction. Gondwana Res. 61, 187–202.

Henderson, C., Baud, A., 1997. Correlation of the Permian–Triassic boundary in Arctic Canada and comparison with Meishan, China. In: Naiwen, W., Remane, J. (Eds.), Proceedings of the 30th International Geological Congress. 11. pp. 143–152 1997.

Hochuli, P.A., Hermann, E., Vigran, J.O., Bucher, H., Weissert, H., 2010. Rapid demise and recovery of plant ecosystems across the end-Permian extinction event. Glob. Planet. Chang. 74 (3–4), 144–155.

Hodell, D.A., Evans, H.F., Channell, J.E., Curtis, J.H., 2010. Phase relationships of North Atlantic ice-rafted debris and surface-deep climate proxies during the last glacial period. Quat. Sci. Rev. 29 (27–28), 3875–3886.

Hofmann, R., Hautmann, M., Bucher, H., 2013. A new paleoecological look at the Dinwoody Formation (Lower Triassic, western US): intrinsic versus extrinsic controls on ecosystem recovery after the end-Permian mass extinction. J. Paleontol. 87, 854–880.

Hofmann, R., Hautmann, M., Brayard, A., Nützel, A., Bylund, K.G., Jenks, J.F., Vennin, E., Olivier, N., Bucher, H., Sevastopulo, G., 2014. Recovery of benthic marine communities from the end-Permian mass extinction at the low latitudes of eastern Panthalassa. Palaeontology 57, 547–589. https://doi.org/10.1111/pala.12076.

Hofmann, R., Hautmann, M., Bucher, H., 2015. Recovery dynamics of benthic marine communities from the Lower Triassic Werfen Formation, northern Italy. Lethaia 48, 474–496. https://doi.org/10.1111/let.12121.

Horacek, M., Richoz, S., Brandner, R., Krystyn, L., Spötl, C., 2007. Evidence for recurrent changes in Lower Triassic oceanic circulation of the Tethys: the δ13C record from marine sections in Iran. Palaeogeogr. Palaeoclimatol. Palaeoecol. 252 (1–2), 355–369.

Huang, C., 2018. Astronomical time scale for the Mesozoic. Stratigraphy & Timescales 3, 81–150.

Ivanov, A.V., He, H., Yan, L., Ryabov, V.V., Shevko, A.Y., Palesskii, S.V., Nikolaeva, I.V., 2013. Siberian Traps large igneous province: evidence for two flood basalt pulses

around the Permo-Triassic boundary and in the Middle Triassic, and contemporaneous granitic magmatism. Earth Sci. Rev. 122, 58–76.

Jafarian, E., Groen, R.D., Nooitgedacht, C.W., Scheibner, C., Blomeier, D., Reijmer, J.J., 2017. Facies arrangement and cyclostratigraphic architecture of the Templet Member and the Kapp Starostin Formation (Permian) on Spitsbergen, Svalbard. Norwegian Journal of Geology/Norsk Geologisk Forening 97 (4), 263–281.

Jaffey, A.H., Flynn, K.F., Glendenin, L.E., Bentley, W.T., Essling, A.M., 1971. Precision measurement of half-lives and specific activities of U 235 and U 238. Physical Review C 4 (5), 1889.

Jelby, M.E., Grundvåg, S.A., Helland-Hansen, W., Olaussen, S., Stemmerik, L., 2020. Tempestite facies variability and storm-depositional processes across a wide ramp: towards a polygenetic model for hummocky cross-stratification. Sedimentology 67 (2), 742–781.

Joachimski, M.M., Lai, X., Shen, S., Jiang, H., Luo, G., Chen, B., ... Sun, Y., 2012. Climate warming in the latest Permian and the Permian–Triassic mass extinction. Geology 40 (3), 195–198.

Joachimski, M.M., Alekseev, A.S., Grigoryan, A., Gatovsky, Y.A., 2020. Siberian Trap volcanism, global warming and the Permian-Triassic mass extinction: new insights from Armenian Permian-Triassic sections. Bulletin 132 (1–2), 427–443.

Kearsey, T., Twitchett, R.J., Price, G.D., Grimes, S.T., 2009. Isotope excursions and palaeotemperature estimates from the Permian/Triassic boundary in the Southern Alps (Italy). Palaeogeogr. Palaeoclimatol. Palaeoecol. 279 (1–2), 29–40.

Kemp, D.B., Eichenseer, K., Kiessling, W., 2015. Maximum rates of climate change are systematically underestimated in the geological record. Nat. Commun. 6, 8890.

Kidder, D.L., Worsley, T.R., 2004. Causes and consequences of extreme Permo-Triassic warming to globally equable climate and relation to the Permo-Triassic extinction and recovery. Palaeogeogr. Palaeoclimatol. Palaeoecol. 203 (3–4), 207–237.

Koevoets, M.J., Abay, T.B., Hammer, Ø., Olaussen, S., 2016. High-resolution organic carbon–isotope stratigraphy of the Middle Jurassic–Lower Cretaceous Agardhfjellet Formation of central Spitsbergen, Svalbard. Palaeogeogr. Palaeoclimatol. Palaeoecol. 449, 266–274.

Korte, C., Kozur, H.W., 2010. Carbon-isotope stratigraphy across the Permian–Triassic boundary: a review. J. Asian Earth Sci. 39 (4), 215–235.

Kozur, H., 1996. The conodonts Hindeodus, Isarcicella and Sweetohindeodus in the uppermost Permian and lowermost Triassic. Geologia Croatica 49 (1), 81–115.

Kozur, H., Pjatakova, M., 1976. The conodont Anchignathodus parvus n. sp., an important guide fossil for the lower Triassic. Proc. K. Ned. Akad. Wet. Ser. B Palaeontol. Geol. Phys. Chem. 79, 123–128.

Laskar, J., Fienga, A., Gastineau, M., Manche, H., 2011. La2010: a new orbital solution for the long-term motion of the Earth. Astronomy & Astrophysics 532, A89.

Lau, K.V., Maher, K., Altiner, D., Kelley, B.M., Kump, L.R., Lehrmann, D.J., Silva-Tamayo, J.C., Weaver, K.L., Yu, M., Payne, J.L., 2016. Marine anoxia and delayed Earth system recovery after the end-Permian extinction. Proc. Natl. Acad. Sci. 113 (9), 2360–2365.

Li, M., Ogg, J., Zhang, Y., Huang, C., Hinnov, L., Chen, Z.Q., Zou, Z., 2016. Astronomical tuning of the end-Permian extinction and the Early Triassic Epoch of South China and Germany. Earth Planet. Sci. Lett. 441, 10–25.

Li, M., Hinnov, L., Kump, L., 2019. Acycle: time-series analysis software for paleoclimate research and education. Comput. Geosci. 127, 12–22.

Lipiarski, I., Čmiel, S.R., 1984. The geological conditions of the occurrence of Carboniferous coal in the northwestern part of Sørkapp Land in West Spitsbergen. Polish Polar Research 5 (3–4), 255–266.

Lord, G.S., Solvi, K.H., Ask, M., Mørk, A., Hounslow, M.W., Paterson, N.W., 2014. The hopen member: a new member of the Triassic De Geerdalen Formation, Svalbard. Norw. Petrol. Direct. Bull. 11 (1), 81–96.

MacEachern, J.A., Bann, K.L., Bhattacharya, J.P., Howell Jr., C.D., 2005. Ichnology of deltas: organism responses to the dynamic interplay of rivers, waves, storms, and tides. In: Gioson, L., Bhattacharya, J.P. (Eds.), River Deltas: Concepts Models and Examples. 83. SEPM Special Publication, pp. 49–85.

MacLeod, K.G., Quinton, P.C., Bassett, D.J., 2017. Warming and increased aridity during the earliest Triassic in the Karoo Basin, South Africa. Geology 45 (6), 483–486.

Major, H., Nagy, J., Haremo, P., Dallmann, W.K., Andersen, A., Salvigsen, O., 1992. Adventdalen. In: Geological Map Svalbard 1:100 000, Sheet C9G. Norsk Polarinstitutt.

Malkowski, K., 1982. Development and stratigraphy of the Kapp Starostin Formation (Permian) of Spitsbergen. Palaeontol. Pol. 43, 69–81.

Mettam, C., Zerkle, A.L., Claire, M.W., Izon, G., Junium, C.J., Twitchett, R.J., 2017. High-frequency fluctuations in redox conditions during the latest Permian mass extinction. Palaeogeogr. Palaeoclimatol. Palaeoecol. 485, 210–223.

Meyer, K.M., Yu, M., Jost, A.B., Kelley, B.M., Payne, J.L., 2011. δ13C evidence that high primary productivity delayed recovery from end-Permian mass extinction. Earth Planet. Sci. Lett. 302 (3–4), 378–384.

Midtkandal, I., Nystuen, J.P., Nagy, J., Mørk, A., 2008. Lower Cretaceous lithostratigraphy across a regional subaerial unconformity in Spitsbergen: the Rurikfjellet and Helvetiafjellet formations. Nor. J. Geol. 88 (4), 287–304.

Mii, H.S., Grossman, E.L., Yancey, T.E., 1997. Stable carbon and oxygen isotope shifts in Permian seas of West Spitsbergen-Global change or diagenetic artifact? Geology 25 (3), 227–230.

Mørk, A., Knarud, R., Worsley, D., 1982. Depositional and diagnetic environments of the Triassic and lower Jurassic succession of Svalbard. In: Embry, A.F., Balkwill, H.R. (Eds.), Arctic Geology and Geophysics, Canadian Society of Petroleum Geologist, Calgary, Alberta, Canada, Memoir. 8. pp. 371–398.

Mørk, A., Embry, A., Weitschat, W., 1989. Triassic transgressive-regressive cycles in the Sverdrup basin, Svalbard and Barents shelf. In: Collinson, J.D. (Ed.), Correlation in Hydrocarbon Exploration, Proceedings of a Norwegian Society Conference, Graham and Trotman, London, pp. 113–130.

Mørk, A., Vigran, J.O., Korchinskaya, M.V., Pchelina, T.M., Fefilova, L.A., Vavilov, M.N.,

Weitschat, W., 1993. Triassic Rocks in Svalbard, the Arctic Soviet Islands and the Barents Shelf: Bearing on Their Correlations. 2. Norwegian Petroleum Society Special Publications, pp. 457–479.

Mørk, A., Elvebakk, G., Forsberg, A.W., Hounslow, M.W., Nakrem, H.A., Vigran, J.O., Weitschat, W., 1999a. The type section of the Vikinghøgda Formation: a new Lower Triassic unit in central and eastern Svalbard. Polar Res. 18 (1), 51–82.

Mørk, A., Dallmann, W.K., Dypvik, H., Johannessen, E.P., Larsen, G.B., Nagy, J., Nøttvedt, A., Olaussen, S., Pcelina, T.M., Worsley, D., 1999b. Mesozoic lithostratigraphy. In: Dallmann (Ed.), Lithostratigraphic Lexicon of Svalbard. Norsk Polarinstitutt, Tromsø, pp. 127–214.

Nabbefeld, B., Grice, K., Twitchett, R.J., Summons, R.E., Hays, L., Böttcher, M.E., Asif, M., 2010. An integrated biomarker, isotopic and palaeoenvironmental study through the Late Permian event at Lusitaniadalen, Spitsbergen. Earth Planet. Sci. Lett. 291 (1–4), 84–96.

Nagy, J., Berge, S.H., 2008. Micropalaeontological evidence of brackish water conditions during deposition of the Knorringfjellet Formation, Late Triassic–Early Jurassic, Spitsbergen. Polar Res. 27 (3), 413–427.

Nakrem, H.A., Mørk, A., 1991. New Early Triassic Bryozoa (Trepostomata) from Spitsbergen, with some remarks on the stratigraphy of the investigated horizons. Geol. Mag. 128 (2), 129–140.

Nakrem, H.A., Orchard, M.J., Weitschat, W., Hounslow, M.W., Beatty, T.W., Mørk, A., 2008. Triassic conodonts from Svalbard and their Boreal correlations. Polar Res. 27 (3), 523–539.

Ogden, D.E., Sleep, N.H., 2012. Explosive eruption of coal and basalt and the end-Permian mass extinction. Proc. Natl. Acad. Sci. 109 (1), 59–62.

Payne, J.L., Lehrmann, D.J., Wei, J., Orchard, M.J., Schrag, D.P., Knoll, A.H., 2004. Large perturbations of the carbon cycle during recovery from the end-Permian extinction. Science 305 (5683), 506–509.

Proemse, B.C., Grasby, S.E., Wieser, M.E., Mayer, B., Beauchamp, B., 2013. Molybdenum isotopic evidence for oxic marine conditions during the latest Permian extinction. Geology 41 (9), 967–970.

Reid, C.M., James, N.P., Beauchamp, B., Kyser, T.K., 2007. Faunal turnover and changing oceanography: Late Palaeozoic warm-to-cool water carbonates, Sverdrup Basin, Canadian Arctic Archipelago. Palaeogeogr. Palaeoclimatol. Palaeoecol. 249 (1–2), 128–159.

Retallack, G.J., Jahren, A.H., 2008. Methane release from igneous intrusion of coal during Late Permian extinction events. The Journal of Geology 116 (1), 1–20.

Rothwell, R.G., Croudace, I.W., 2015. Twenty years of XRF core scanning marine sediments: what do geochemical proxies tell us? In: Croudace, I.W., Rothwell, R.G. (Eds.), Micro-XRF Studies of Sediment Cores. Springer, Dordrecht, pp. 25–102.

Rothwell, R.G., Rack, F.R., 2006. New techniques in sediment core analysis: an introduction. In: Rothwell, R.G. (Ed.), New Techniques in Sediment Core Analysis, Geological Society, London, Special Publication. 267. pp. 1–29.

Sanchez-Lorenzo, A., Enriquez-Alonso, A., Calbó, J., González, J.A., Wild, M., Folini, D., ... Vicente-Serrano, S.M., 2017. Fewer clouds in the Mediterranean: consistency of observations and climate simulations. Scientific reports 7, 41475.

Sanson-Barrera, A., Hochuli, P.A., Bucher, H., Schneebeli-Hermann, E., Weissert, H., Adatte, T., Bernasconi, S.M., 2015. Late Permian–earliest Triassic high-resolution organic carbon isotope and palynofacies records from Kap Stosch (East Greenland). Glob. Planet. Chang. 133, 149–166.

Schobben, M., Joachimski, M.M., Korn, D., Leda, L., Korte, C., 2014. Palaeotethys seawater temperature rise and an intensified hydrological cycle following the end-Permian mass extinction. Gondwana Res. 26 (2), 675–683.

Schobben, M., Foster, W.J., Sleveland, A.R.N., Zuchuat, V., Svensen, H., Planke, S., Bond, D.P.G., Marcelis, F., Newton, R.J., Wignall, P.B., Poulton, S.W., 2020. A nutrient-driven tipping point catalysed marine anoxia during the end-Permian mass extinction. Nat. Geosci (in press).

Schmitz, M.D., Schoene, B., 2007. Derivation of isotope ratios, errors, and error correlations for U-Pb geochronology using 205Pb-235U-(233U)-spiked isotope dilution thermal ionization mass spectrometric data. Geochem. Geophys. Geosyst. 8 (8).

Seidler, L., Steel, R., Stemmerik, L., Surlyk, F., 2004. North Atlantic marine rifting in the Early Triassic: new evidence from East Greenland. J. Geol. Soc. 161 (4), 583–592.

Smelror, M., Larssen, G.B., 2016. Are there Upper Cretaceous sedimentary rocks preserved on Sørkapp Land, Svalbard? Nor. J. Geol. 96 (2), 1–12.

Smelror, M., Petrov, O.V., Larssen, G.B., Werner, S.C., 2009. Geological History of the Barents Sea. Geological Survey of Norway, Trondheim (135 pp).

Smith, R.M., Botha-Brink, J., 2014. Anatomy of a mass extinction: sedimentological and taphonomic evidence for drought-induced die-offs at the Permo-Triassic boundary in the main Karoo Basin, South Africa. Palaeogeogr. Palaeoclimatol. Palaeoecol. 396, 99–118.

Stanley, S.M., 2016. Estimates of the magnitudes of major marine mass extinctions in earth history. Proc. Natl. Acad. Sci. 113 (42), 6325–6334.

Staten, P.W., Lu, J., Grise, K.M., Davis, S.M., Birner, T., 2018. Re-examining tropical expansion. Nat. Clim. Chang. 8 (9), 768.

Stordal, F., Svensen, H.H., Aarnes, I., Roscher, M., 2017. Global temperature response to century-scale degassing from the Siberian Traps large igneous province. Palaeogeogr. Palaeoclimatol. Palaeoecol. 471, 96–107.

Svensen, H., Planke, S., Polozov, A.G., Schmidbauer, N., Corfu, F., Podladchikov, Y.Y., Jamtveit, B., 2009. Siberian gas venting and the end-Permian environmental crisis. Earth Planet. Sci. Lett. 277 (3–4), 490–500.

Svensen, H.H., Frolov, S., Akhmanov, G.G., Polozov, A.G., Jerram, D.A., Shiganova, O.V., Melnikov, M.V., Iyer, K., Planke, S., 2018. Sills and gas generation in the Siberian Traps. Philos. Trans. R. Soc. A Math. Phys. Eng. Sci. 376 (2130), 20170080.

Tozer, E.T., 1965. Lower Triassic stages and ammonoid zones of Arctic Canada. Geol. Surv. Can. Pap. 65 (12), 1–11.

Tozer, E.T., 1967. A standard for Triassic time. Geological Survey of Canada Bulletin 156, 1–103.

Tribovillard, N., Algeo, T.J., Lyons, T., Riboulleau, A., 2006. Trace metals as paleoredox and paleoproductivity proxies: an update. Chem. Geol. 232 (1–2), 12–32.

Twitchett, R.J., Looy, C.V., Morante, R., Visscher, H., Wignall, P.B., 2001. Rapid and synchronous collapse of marine and terrestrial ecosystems during the end-Permian biotic crisis. Geology 29 (4), 351–354.

Uchman, A., Hanken, N.M., Nielsen, J.K., Grundvåg, S.A., Piasecki, S., 2016. Depositional environment, ichnological features and oxygenation of Permian to earliest Triassic marine sediments in central Spitsbergen, Svalbard. Polar Res. 35 (1), 24782.

van Soelen, E.E., Twitchett, R., Kürschner, W.M., 2018. Salinity changes and anoxia resulting from enhanced run-off during the late Permian global warming and mass extinction event. Clim. Past 14, 441–453.

Viglietti, P.A., Smith, R.M., Rubidge, B.S., 2018. Changing palaeoenvironments and tetrapod populations in the Daptocephalus Assemblage Zone (Karoo Basin, South Africa) indicate early onset of the Permo-Triassic mass extinction. J. Afr. Earth Sci. 138, 102–111.

Vigran, J.O., Mangerud, G., Mørk, A., Worsley, P.A., Hochuli, P.A., 2014. Palynology and geology of the Triassic succession on Svalbard and the Barents Sea. Geological Survey of Norway Special Publication 14, 1–272.

Walker, R.G., 1992. Facies, facies models and modern stratigraphic concepts. In: Walker, R.G., James, N.P. (Eds.), Facies Models: Response to Sea-Level Change, Geological Association of Canada, pp. 1–14.

Waltham, D., 2015. Milankovitch period uncertainties and their impact on cyclostratigraphy. J. Sediment. Res. 85 (8), 990–998. Available at. http://nm2.rhul.ac.uk/wp-content/uploads/2015/01/Milankovitch.html.

Wand, M.P., Jones, M.C., 1994. Kernel Smoothing. Chapman & Hall/CRC Press, London.

Wang, Y., Sadler, P.M., Shen, S.Z., Erwin, D.H., Zhang, Y.C., Wang, X.D., ... Henderson, C.M., 2014. Quantifying the process and abruptness of the end-Permian mass extinction quantifying the end-Permian mass extinction. Paleobiology 40 (1), 113–129.

Wang, X., Cawood, P.A., Zhao, H., Zhao, L., Grasby, S.E., Chen, Z.Q., Zhang, L., 2019. Global mercury cycle during the end-Permian mass extinction and subsequent Early Triassic recovery. Earth Planet. Sci. Lett. 513, 144–155.

Ware, D., Jenks, J.F., Hautmann, M., Bucher, H., 2011. Dienerian (Early Triassic) ammonoids from the Candelaria Hills (Nevada, USA) and their significance for palaeobiogeography and palaeoceanography. Swiss J. Geosci. 104 (1), 161–181.

Wendorff, M., 1985. Geology of the Palffyodden area (NW Sorkappland, Spitsbergen): course and some results of investigations in 1982. Zeszyty Naukowe UJ, Prace Geograficz 63, 33–55.

Wignall, P.B., Twitchett, R.J., 1996. Oceanic anoxia and the end Permian mass extinction. Science 272 (5265), 1155–1158.

Wignall, P.B., Twitchett, R.J., 2002. Permian–Triassic sedimentology of Jameson Land, East Greenland: incised submarine channels in an anoxic basin. J. Geol. Soc. 159 (6), 691–703.

Wignall, P.B., Morante, R., Newton, R., 1998. The Permo-Triassic transition in Spitsbergen: δ 13 C org chemostratigraphy, Fe and S geochemistry, facies, fauna and trace fossils. Geol. Mag. 135 (1), 47–62.

Wignall, P.B., Bond, D.P., Sun, Y., Grasby, S.E., Beauchamp, B., Joachimski, M.M., Blomeier, D.P., 2016. Ultra-shallow-marine anoxia in an Early Triassic shallow-marine clastic ramp (Spitsbergen) and the suppression of benthic radiation. Geol. Mag. 153 (2), 316–331.

Woitke, P., Wellmitz, J., Helm, D., Kube, P., Lepom, P., Litheraty, P., 2003. Analysis and assessment of heavy metal pollution in suspended solids and sediments of the river Danube. Chemosphere 51 (8), 633–642.

Woods, A.D., 2005. Paleoceanographic and paleoclimatic context of Early Triassic time. Comptes Rendus Palevol 4 (6–7), 463–472.

Worsley, D., 2008. The post-Caledonian development of Svalbard and the western Barents Sea. Polar Res. 27 (3), 298–317.

Worsley, D., Mørk, A., 1978. The Triassic stratigraphy of southern Spitsbergen. Norsk Polarinstitutt Årbok 1977, 43–60.

Yin, H., Zhang, K., Tong, J., Yang, Z., Wu, S., 2001. The Global Stratotype Section and Point (GSSP) of the Permian-Triassic boundary. Episodes 24, 02–114.

Zuchuat, V., 2014. A Sedimentary Investigation of the Lower Triassic Formations and Their Underlying Permo-Carboniferous Units Across Spitsbergen, Svalbard. Master's thesis. Department of Geology and Mineral Resources Engineering, Norwegian University of Science and Technology, Norway, pp. 1–167.